Mon. Not. R. Astron. Soc. **000**, 1–?? (2012) Printed 14 January 2015 (MN LATEX style file v2.2)

PTF11iqb: Cool supergiant mass loss that bridges the gap between Type IIn and normal supernovae

Nathan Smith[1⋆], Jon C. Mauerhan[1,2], S. Bradley Cenko[3], Mansi M. Kasliwal[4], Jeffrey M. Silverman[5], Alexei V. Filippenko[2], Avishay Gal-Yam[6], Kelsey I. Clubb[2], Melissa L. Graham[2], Douglas C. Leonard[7], J. Chuck Horst[7], G. Grant Williams[1,8], Jennifer E. Andrews[1], Shrinivas R. Kulkarni[4], Peter Nugent[2,9], Mark Sullivan[10], Kate Maguire[11], Dong Xu[6], and Sagi Ben-Ami[6]

[1] *Steward Observatory, University of Arizona, 933 N. Cherry Ave., Tucson, AZ 85721, USA*
[2] *Department of Astronomy, University of California, Berkeley, CA 94720-3411, USA*
[3] *Astrophysics Science Division, NASA Goddard Space Flight Center, Mail Code 661, Greenbelt, MD 20771*
[4] *Astronomy Department, California Institute of Technology, 1200 E. California Boulevard, Pasadena, CA 91125, USA*
[5] *Department of Astronomy, University of Texas, Austin, TX 78712, USA*
[6] *Department of Particle Physics and Astrophysics, Weizmann Institute of Science, Rehovot 76100, Israel*
[7] *Department of Astronomy, San Diego State University, San Diego, CA 92182-1221*
[8] *MMT Observatory, Tucson, AZ 85721-0065, USA*
[9] *Computational Research Division, Lawrence Berkeley National Laboratory, 1 Cyclotron Road MS 50B-4206, Berkeley, CA 94720, USA*
[10] *School of Physics and Astronomy, University of Southampton, Southampton SO17 1BJ, UK*
[11] *European Southern Observatory for Astronomical Research in the Southern Hemisphere (ESO), Karl-Schwarzschild-Str. 2, 85748 Garching b. München, Germany*

14 January 2015

ABSTRACT

The supernova (SN) PTF11iqb was initially classified as a Type IIn event caught very early after explosion. It showed narrow Wolf-Rayet (WR) spectral features on day 2 (as in SN 1998S and SN 2013cu), but the narrow emission weakened quickly and the spectrum morphed to resemble those of Types II-L and II-P. At late times, Hα emission exhibited a complex, multipeaked profile reminiscent of SN 1998S. In terms of spectroscopic evolution, we find that PTF11iqb was a near twin of SN 1998S, although with a factor of ~ 2–4 weaker interaction with circumstellar material (CSM) at early times, and stronger CSM interaction at late times. We interpret the spectral changes as caused by early interaction with asymmetric CSM that is quickly (by day 20) enveloped by the expanding SN ejecta photosphere, but then revealed again after the end of the plateau when the photosphere recedes. The light curve can be matched with a simple model for weak CSM interaction (with a mass-loss rate of roughly $10^{-4}\,M_{\odot}$ yr^{-1}) added to the light curve of a normal SN II-P; the relatively weak CSM interaction allows the plateau to be seen more clearly than in other SNe IIn. This plateau requires that the progenitor had an extended hydrogen envelope like a red supergiant at the moment that it exploded, consistent with the slow progenitor wind speed (< 80 km s^{-1}) indicated by narrow Hα emission. The cool supergiant progenitor is significant because PTF11iqb showed WR features in its early spectrum — meaning that the presence of such WR features in an early SN spectrum does not necessarily indicate a WR-like progenitor. While the late-time Hα profile was multipeaked and asymmetric like that of SN 1998S, PTF11iqb's Hα developed a stronger *redshifted* peak, so in this case the asymmetry cannot be blamed on dust obscuration. Instead, azimuthal asymmetry due to binary interaction is likely. Overall, PTF11iqb bridges SNe IIn with weaker pre-SN mass loss seen in SNe II-L and II-P, implying a continuum between these types. It hints at episodic pre-SN mass loss on a wider scale than previously recognised.

Key words: circumstellar matter — stars: evolution — stars: winds, outflows — supernovae: general — supernovae: individual (PTF11iqb)

1 INTRODUCTION

Recent years have seen the growing recognition that episodic mass loss may be a critical ingredient in the evolution of massive stars. Perhaps the most vivid demonstration is the class of Type IIn supernovae (SNe), which have narrow emission lines (Schlegel 1990; Filippenko 1997) arising from extremely dense circumstellar material (CSM) that is close to the star and must have been ejected in only the few years or decades preceding the final explosion; see Smith (2014) for a general review of massive-star mass loss and its connection to SN diversity.

The synchronisation of this episodic mass loss occurring such a short time before core collapse suggests that it is connected to some instability in the latest stages of nuclear burning — most likely during Ne, O, and Si burning, but perhaps also C burning on longer timescales (Quataert & Shiode 2012; Shiode & Quataert 2014; Smith & Arnett 2014). Some SNe have associted precursor eruptions detected in the few years before explosion (Foley et al. 2007; Pastorello et al. 2007; Smith et al. 2010a; Mauerhan et al. 2013a; Corsi et al. 2014; Fraser et al. 2013; Ofek et al. 2013a, 2014a). Since stars may alter their structure shortly before core collapse, this makes it challenging to connect SNe to the properties of traditional populations of evolved stars.

Eruptions driven by the pulsational pair-instability (PPI; Rakavy & Shaviv 1967) have been suggested as a possible physical cause of some of this violent late-phase mass loss (e.g., Woosley et al. 2007). While the PPI could potentially be important in the most extreme and rare events like superluminous SNe IIn that require ejection of 10–20 $M_\odot$ (e.g., Smith et al. 2008a, 2010b; Ofek et al. 2014b; Gal-Yam 2012; Zhang et al. 2012), the requirements on the very high initial mass of a PPI progenitor ($\sim 100\,M_\odot$; Heger et al. 2003) as well as a preference for low metallicity indicate that such events must be far too rare to account for the general population of SNe IIn (Smith et al. 2011a; Smith & Arnett 2014; Smith, Mauerhan, & Prieto 2014). Multidimensional numerical simulations of the latest phases of nuclear burning in massive stars reveal instabilities that may be more widespread (i.e., in lower-mass stars of 20–30 $M_\odot$), and might lead to violent eruptive mass loss (Arnett & Meakin 2011). Quataert & Shiode (2012) suggested that these latest phases of Ne and O burning might induce wave-driven mass loss that could contribute (see also Shiode & Quataert 2014). A number of other possibilities may exist as well: Smith & Arnett (2014) pointed out that even if waves propagating out from the core are insufficient to cause hydrodynamic mass loss on their own, their dissipation in the envelope may cause a pulsation or inflation of the star, perhaps triggering a collision with a companion star in a binary system that had previously been safely separated. Moreover, violent convection and mixing in the final phases may be able to trigger explosive nuclear burning that could cause sudden energy deposition. In any case, the empirical fact that some SNe experience violent eruptive mass loss in their latest burning phases indicates that the stellar structure may be significantly modified compared to the endpoints of one-dimensional stellar-evolution models; Smith & Arnett (2014) proposed that this could be an extremely important consideration in understanding core collapse (i.e., pre-explosion disruption of the core structure might make some stars *easier* to explode).

SNe IIn contribute a fraction of 8–9% of all core-collapse SNe (Smith et al. 2011a) in a volume-limited sample of large star-forming galaxies, and there are hints that they are as common or possibly more common at lower metallicity (see Smith 2014). It is interesting that $\sim 10\%$ of core-collapse SNe exhibit vivid warnings of their impending core collapse in the form of violent fits of dynamic mass loss, while the vast majority of normal SNe do not. An open question is whether explosions classified as SNe IIn are the only massive stars that experience pre-SN instability, *or if they are just the most extreme expression of a more generic instability operating in a larger fraction of massive stars*. Whereas the PPI is indeed limited to a small fraction of the most massive stars, wave-driven mass loss, inflation of the star that triggers collisions with a companion star, and explosive burning may be more generic and may operate over a wide range of mass. Quantitative expectations of the energy deposition and mass loss from theory are still uncertain, but one can imagine that there is a substantial range in both. If there is a range in energy deposition from pre-SN instability, there may also be a continuum in CSM density, from the most violent SNe IIn down to normal winds. Anecdotally, it is already clear that SNe IIn exhibit a wide range of CSM mass with diverse radial density structure and geometry. They can eject as much as 10–20 $M_\odot$ in the cases of rare superluminous SNe IIn (see above), 0.1–1 $M_\odot$ in more common SNe IIn (Kiewe et al. 2012; Ofek et al. 2013b; Taddia et al. 2013), and they even have CSM that could arise from the dense winds of extreme red supergiants (RSGs; Smith et al. 2009a,b; Mauerhan & Smith 2012; Stritzinger et al. 2012).

In this paper, we report evidence that the Type IIn phenomenon may extend to even lower mass-loss scales, in SNe that are recognised as Type IIn *only if they are caught early enough after explosion*, and then transition into more normal SN types as they age. Thus, some other "normal" SNe might also experience pre-SN instability akin to SNe IIn, but less extreme in scale or more limited in duration. In the title of this paper and throughout the text, we refer to "normal" SNe as those which are not seen to be strongly interacting based on their visible-wavelength spectra (SNe Ibc, IIb, II-P, II-L; see Filippenko 1997 for a review), where the visual-wavelength spectrum is dominated by the receding photosphere that is located within the fast freely expanding SN ejecta, and not in the shock/CSM interaction region. Thus, normal SNe in this context exclude Types IIn and Ibn. Signs of weaker CSM interaction have often been seen in X-ray and radio emission (Chevalier & Fransson 1994; Fransson et al. 1996; Murase et al. 2014).

We present visual-wavelength photometry and spectroscopy of PTF11iqb taken from the time of first detection up to $\sim$ 1100 days afterward. PTF11iqb was discovered (Parrent et al. 2011) at $R = 16.8$ mag by the Palomar Transient Factory (PTF; Law et al. 2009; Rau et al. 2009) on 2011 July 23 (UTC dates are used throughout this paper) in an inner spiral arm of the nearby barred spiral galaxy NGC 151 (see Figure 1), and was initially classified as having a Type IIn spectrum (as we discuss below, however, the spectral evolution became complicated). Based on the redshift of $z = 0.0125$ (3750 km s^{-1}), we adopt a distance of 50.4 Mpc ($m - M = 33.51$ mag), and a Milky Way line-of-sight

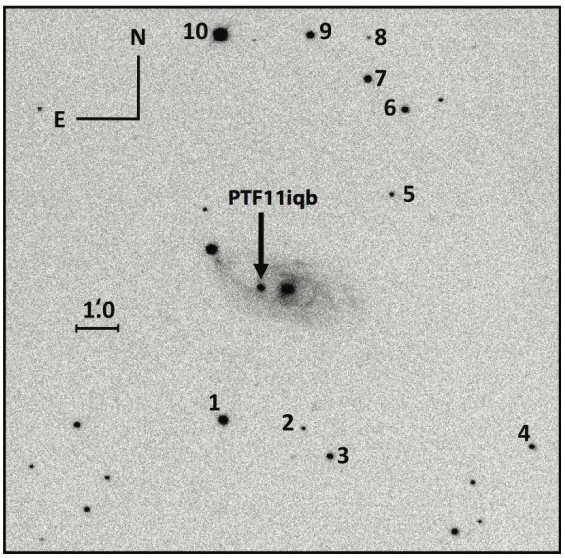

Figure 1. *B*-band image of NGC 151 taken on 2011 August 5 with the Mount Laguna Observatory 40-inch reflecting telescope. PTF11iqb is indicated by the arrow. The local standards listed in Table 3 are marked.

reddening of $E(B-V) = 0.0284$ mag (Schlegel et al. 1998). PTF11iqb resides in the bright inner region of NGC 151, in the ring surrounding the central bar, at a projected separation of $\sim 30''$ ($\sim$ 7–8 kpc) from the host galaxy's nucleus. Early reports indicated nondetections of PTF11iqb in X-rays (Quimby et al. 2011) and radio (Horesh et al. 2011). Later, PTF11iqb exhibited a marginal X-ray detection at $\sim$ 24 days after peak, and then another non-detection 28 days after peak, which was suggested to indicate a relatively low ratio of the X-ray luminosity to visual-wavelength luminosity, as compared to other SNe IIn (Ofek et al. 2013b). Our new observations are presented in §2, and the light curve and spectral evolution are analyzed in §3. We compare PTF11iqb with SN 1998S in §4, and in §5 we present a simple CSM interaction model. In §6 we discuss the late-time Hα and in §7 we discuss the WR features seen in the early-time spectrum. Section 8 presents an overview and summary, and we discuss PTF11iqb in context with other SNe IIn and normal (noninteracting) Type II (II-P and II-L) SNe.

Table 1. P48 photometry[a]

MJD	R (mag)	σ (mag)
55765.4	16.862	0.036
55765.4	16.834	0.039
55766.4	16.135	0.049
55766.4	16.073	0.050
55768.4	15.608	0.027
55768.4	15.603	0.050
55769.4	15.462	0.047
55769.4	15.458	0.050
55770.4	15.370	0.040
55770.4	15.323	0.057
55771.4	15.291	0.047
55771.4	15.265	0.057
55774.3	15.218	0.048
55774.4	15.194	0.054
55775.5	15.147	0.072
55779.4	15.194	0.050
55779.5	15.178	0.056
55780.4	15.169	0.054
55780.5	15.180	0.069
55782.4	15.204	0.060
55782.4	15.193	0.076
55783.3	15.247	0.025
55783.4	15.258	0.034
55784.3	15.274	0.028
55784.4	15.274	0.051
55793.3	15.482	0.041
55794.3	15.486	0.043
55811.3	15.789	0.047
55811.3	15.776	0.056
55812.2	15.779	0.044
55813.3	15.822	0.049
55813.4	15.807	0.055
55821.2	15.909	0.052
55821.3	15.899	0.058
55822.2	15.921	0.046
55822.3	15.923	0.062
55823.2	15.921	0.049
55823.3	15.908	0.062
55824.3	15.939	0.055
55824.3	15.897	0.070
55838.2	16.054	0.050
55842.3	16.082	0.039
55842.3	16.085	0.033
55850.2	16.137	0.051
55850.2	16.134	0.055
55851.2	16.154	0.053
55851.2	16.160	0.049
55852.2	16.144	0.067
55852.3	16.159	0.072
55853.2	16.169	0.066
55853.3	16.186	0.059
55854.2	16.131	0.064
55854.3	16.137	0.072

[a]Mould *R* filter

2 OBSERVATIONS

2.1 Palomar 48-inch Discovery and Photometry

We obtained *R*-band images of the PTF11iqb field including NGC 151 on 2011 July 22.37 with the Palomar 48-inch telescope (P48) equipped with the refurbished CFHT12k camera (Rahmer et al. 2008). Subtraction of a stacked reference image of the field with HOTPANTS[1] revealed a new transient source at coordinates $\alpha = 00^{\rm h}34^{\rm m}04\overset{\rm s}{.}84$, $\delta = -09°42''17\overset{''}{.}9$ (J2000.0), with an astrometric uncertainty (relative to the USNO-B1 catalog; Monet et al. 2003) of $\pm$150 mas in each coordinate. The transient was discovered 30 hours later by Oarical, an autonomous software framework of the PTF collaboration (Bloom et al. 2011). It was classified correctly as a transient source (as opposed to a variable star), was further classified as a SN or nova, and was given the name PTF11iqb. No source was detected at this location with P48 in an image taken on 2011 Jul 17.5, to a 3σ limit of $R \approx 18.5$ mag (see Figures 2 and 3).

Our photometric pipeline has been used in many previous PTF papers (e.g., Firth et al. 2015; Ofek et al. 2012, 2014a; Pan et al. 2014; Laher et al. 2014), and is based on image subtraction. We construct a deep reference image from data prior to the SN explosion, register this reference to each image containing the SN light, match the point spread functions (PSFs), perform the image subtraction, and then measure the SN flux using PSF photometry on the difference images. The PSF is determined using isolated stars in the unsubtracted images, and the image subtraction uses a

[1] http://www.astro.washington.edu/users/becker/hotpants.htm

nonparametric pixelised kernel (similar to that in Bramich 2008). The average PSF is then fit at the position of the SN event weighting each pixel according to Poisson statistics, yielding a SN flux and flux uncertainty. We flux calibrate our P48 light curve to the Sloan Digital Sky Survey (SDSS; York et al. 2000) Data Release 10 (DR10; Ahn et al. 2014). The resulting magnitudes are given in Table 1 and are shown in Figures 2 and 3.

2.2 Palomar 60-inch Photometry

Upon discovery of PTF11iqb, the field was automatically inserted into the queue of the robotic Palomar 60-inch telescope (P60; Cenko et al. 2006) for multifilter (r' and i') follow-up observations. Images were processed using a custom pipeline, and subtracted from reference images obtained in 2014 July using HOTPANTS. The resulting subtracted images were photometrically calibrated using nearby point sources from the SDSS DR10 (Ahn et al. 2014)), so reported magnitudes are on the AB system (Oke & Gunn 1983). A log of P60 photometry is provided in Table 2. The light curve, combining the P48 R-band and the P60 r' and i' photometry, is shown in Figures 2 and 3.

The general rate of fading in P60 ri data is very consistent with the P48 R-band data. However, there are some differences that can mostly be attributed to different amounts of Hα emission in the r (Sloan) and R (Mould) filters, and none in the i filter. We also include a number of i-band upper limits at late times around days 500–600.

2.3 Mount Laguna $BVRI$ Photometry

All photometric data were collected using the Mount Laguna Observatory (MLO; Smith & Nelson 1969) 40-inch reflecting telescope, which is equipped with a 2048×2048 pixel CCD camera (manufactured by Fairchild Imaging Systems; CCD447) located at the $f/7.6$ Cassegrain focus, providing a field of view of approximately $13.5' \times 13.5'$ with $0.41''$ pixel^{-1}. The "seeing," estimated from the full width at half-maximum intensity (FWHM) of stars on the CCD frame, was generally $\sim 2''$, and exposure times of 5 to 30 minutes were typical for the observations, which were taken in the standard Johnson-Cousins (Johnson et al. 1966; Cousins 1981) $BVRI$ bandpasses.

CCD frames were flatfielded using either twilight-sky or dome flats in the usual manner, and cosmic rays were removed using the L.A. Cosmic (van Dokkum 2001) algorithm. Considerable fringing remained in I-band images that did not properly flatten, likely produced by the varying intensity of night-sky emission lines. This has minimal impact on the photometry since both the SN and the comparison stars were much brighter than the background.

Figure 1 shows an MLO B-band image of NGC 151 taken on 2011 August 5, with 10 "local standards" identified in the field of PTF11iqb, which were used to measure the relative SN brightness on nonphotometric nights. The absolute calibration of the field was accomplished on the photometric night of 2012 November 19 by observing several fields of Landolt (1992) standards over a range of airmasses. The derived $BVRI$ magnitudes of the stars are given in Table 3, along with the estimated uncertainties. The transformation coefficients to the standard Johnson-Cousins systems were derived using the solutions from this night. We determined the instrumental magnitudes for the standards using aperture photometry with the IRAF[2] DAOPHOT package (Stetson 1987, 1991), which yielded colour terms for the MLO observations of the form

$$\begin{aligned} B &= b + 0.093\,(B-V) + C_B, \\ V &= v - 0.067\,(B-V) + C_V, \\ R &= r + 0.093\,(V-R) + C_R, \\ I &= i + 0.005\,(V-I) + C_I, \end{aligned} \tag{1}$$

where $bvri$ are the instrumental and $BVRI$ the standard Johnson-Cousins magnitudes. The terms C_B, C_V, C_R, and C_I are the differences between the zero-points of the instrumental and standard magnitudes, determined for each observation by measuring the offset between the instrumental and standard magnitudes and colours of local standards.

We determined the instrumental magnitudes for PTF11iqb and the local standards using the point-spread function (PSF) fitting technique within DAOPHOT (Stetson 1991, and references therein). We used only the inner core of PTF11iqb and the local standards to fit the PSF in order to reduce errors that can be introduced when there is a strong gradient in the background (e.g., Schmidt et al. 1993). In practice, this core was generally set to be about the FWHM of a given image. While the fitting radius of the SN and comparison stars was varied from night to night to match the seeing, the sky background of the SN and local standards was always set to an annulus with a radius of 20–30 pixels ($8\farcs2$–$12\farcs3$) to maintain consistency throughout the observations. We next subtracted the mode of the sky background[3] to derive the instrumental magnitudes for the SN and local standards. The transformation to the standard Johnson-Cousins system was then accomplished using the colour terms listed in Equation 1 and the standard magnitudes of the local standards given in Table 3. On the two nights where images in all four filters were not obtained, for the purpose of estimating the appropriate colour term the colour of PTF11iqb was estimated through interpolation or extrapolation from temporally nearby values; since the colour terms are small, this approximation should have little impact on the resulting photometry.

The final reported photometry was accomplished by taking the simple mean of the values obtained using each of the available calibrator stars on a given night; not all stars were available on all nights, owing either to field-of-view limitations or saturation. The results of our photometric observations are given in Table 4 and shown in Figure 2. The reported uncertainties come from two sources. First, there is the photometric uncertainty reported by the error-analysis package in DAOPHOT from the statistics of the SN and background region. Second, there is uncertainty in the transformation to the standard system. We estimate the

[2] IRAF is distributed by the National Optical Astronomy Observatories, which are operated by the Association of Universities for Research in Astronomy, Inc., under cooperative agreement with the National Science Foundation.

[3] See Da Costa (1992) for a discussion of the advantages of using the mode of the background region rather than the mean or median.

Table 2. P60 r and i photometry of PTF11iqb[a]

MJD	Filt.	mag	σ	MJD	Filt.	mag	σ
55766.449	r	16.134	0.004	55768.358	i	15.948	0.076
55770.355	r	15.347	0.004	...	i	...	...
55774.344	r	15.230	0.004	55774.343	i	15.445	0.035
55776.338	r	15.236	0.004	55776.337	i	15.460	0.069
55776.340	r	15.217	0.004	55776.339	i	15.464	0.053
55778.331	r	15.374	0.004	55778.330	i	15.486	0.107
55778.334	r	15.255	0.004	55778.333	i	15.441	0.067
55780.330	r	15.396	0.003	...	i	...	...
55782.321	r	15.357	0.004	55782.320	i	15.460	0.063
55782.323	r	15.306	0.004	55782.322	i	15.473	0.097
55792.482	r	15.417	0.004	55792.481	i	15.720	0.097
55794.300	r	15.557	0.004	...	i	...	...
55794.300	r	15.704	0.004	...	i	...	...
55796.282	r	15.633	0.004	55796.281	i	15.763	0.049
55798.300	r	15.839	0.004	...	i	...	...
55800.373	r	15.593	0.004	55800.372	i	15.825	0.046
55801.400	r	15.779	0.005	...	i	...	...
55802.300	r	15.616	0.004	...	i	...	...
55803.264	r	15.821	0.004	55803.263	i	15.948	0.040
55804.261	r	15.936	0.004	55804.260	i	15.932	0.070
55805.259	r	15.815	0.004	55805.258	i	15.986	0.084
55806.256	r	15.842	0.005	...	i	...	...
...	r	...	...	55807.254	i	15.935	0.049
55808.251	r	15.888	0.054	55808.250	i	16.033	0.066
55809.400	r	15.807	0.005	...	i	...	...
55811.244	r	15.904	0.005	55811.243	i	16.005	0.058
55812.239	r	15.965	0.005	55812.238	i	16.090	0.076
55813.200	r	15.881	0.006	...	i	...	...
55814.233	r	15.725	0.007	55814.232	i	16.151	0.042
55820.257	r	16.005	0.006	55820.256	i	16.253	0.059
55821.216	r	15.887	0.006	55821.215	i	16.248	0.066
55827.229	r	16.107	0.005	55827.228	i	16.344	0.061
55828.223	r	16.060	0.005	55828.222	i	16.379	0.052
55829.200	r	16.036	0.006	...	i	...	...
55830.200	r	16.265	0.006	...	i	...	...
55831.188	r	16.278	0.158	55831.187	i	16.381	0.050
55832.211	r	16.165	0.006	55832.210	i	16.341	0.063
55833.200	r	16.080	0.006	55833.181	i	16.326	0.048
55834.179	r	16.1220	0.006	55834.178	i	16.380	0.086
55835.177	r	16.076	0.005	55835.176	i	16.358	0.048
55837.300	r	16.425	0.005	...	i	...	...
55838.168	r	16.551	0.007	55838.167	i	16.616	0.050
...	r	...	...	55847.144	i	16.598	0.058
55848.141	r	16.310	0.008	55848.140	i	16.524	0.047
55849.137	r	16.219	0.008	55849.136	i	16.594	0.062
55850.139	r	16.210	0.006	55850.138	i	16.639	0.058
55851.133	r	16.135	0.006	55851.132	i	16.597	0.085
55852.129	r	16.176	0.006	55852.128	i	16.630	0.064
55852.200	r	16.208	0.005	...	i	...	...
55853.130	r	16.323	0.006	55853.129	i	16.640	0.067
55854.129	r	16.330	0.006	55854.128	i	16.687	0.086
55856.100	r	16.324	0.006	...	i	...	...
55857.100	r	16.269	0.006	...	i	...	...
55858.100	r	16.154	0.006	...	i	...	...
...	r	...	...	55859.123	i	16.813	0.053
55862.113	r	16.555	0.007	55862.112	i	16.852	0.062
55863.111	r	16.481	0.007	55863.110	i	16.792	0.041
55864.100	r	16.401	0.007	...	i	...	...
55866.110	r	16.422	0.007	55866.109	i	16.868	0.069
55867.100	r	16.467	0.009	...	i	...	...
55868.105	r	16.693	0.008	55868.104	i	16.952	0.060
55869.100	r	16.509	0.012	...	i	...	...
55874.297	r	16.533	0.014	55874.296	i	17.083	0.065
55884.100	r	16.892	0.012	...	i	...	...
55889.112	r	17.194	0.010	55889.111	i	18.203	0.069
55891.296	r	17.411	0.016	...	i	...	...
55893.157	r	17.576	0.016	55893.156	i	18.604	0.075
...	r	...	...	55895.094	i	18.620	0.074
55902.247	r	17.524	0.024	55902.245	i	18.907	0.081
55903.112	r	17.927	0.017	55903.110	i	18.836	0.058
...	r	...	...	55904.109	i	18.903	0.078
...	r	...	...	55905.105	i	(19.76)	...
55906.276	r	17.595	0.020	55906.274	i	19.040	0.095
55916.133	r	17.537	0.016	55916.131	i	19.120	0.099
...	r	...	...	56290.090	i	(21.69)	...
56296.100	r	20.647	0.332	...	i	...	...
56297.140	r	20.617	0.131	56297.139	i	(21.86)	...
56298.115	r	20.723	0.109	56298.113	i	(22.33)	...
56301.084	r	20.673	0.111	56301.081	i	(21.91)	...
56302.107	r	21.423	1.151	56302.106	i	(19.96)	...
56324.100	r	20.660	0.211	56324.128	i	(22.19)	...
...	r	...	...	56325.129	i	(20.21)	...
56328.115	r	21.129	0.165	56328.113	i	(21.92)	...
56330.112	r	21.142	0.173	56330.110	i	(22.03)	...

[a]Magnitudes in parenthesis indicate upper limits.

Table 3. MLO Magnitudes of Local Standards

Star	B (σ_B)	V (σ_V)	R (σ_R)	I (σ_I)
1	13.822(0.040)	13.258(0.022)	12.873(0.033)	12.563(0.033)
2	17.192(0.052)	16.319(0.027)	15.709(0.039)	15.192(0.040)
3	15.522(0.040)	14.898(0.022)	14.408(0.033)	14.019(0.033)
4	16.091(0.040)	14.796(0.022)	13.859(0.033)	13.129(0.033)
5	16.856(0.045)	15.714(0.023)	14.949(0.035)	14.250(0.034)
6	15.253(0.040)	14.511(0.022)	14.025(0.033)	13.591(0.033)
7	14.883(0.040)	14.214(0.022)	13.823(0.033)	13.446(0.033)
8	17.893(0.065)	16.660(0.029)	15.858(0.042)	15.055(0.042)
9	14.702(0.040)	14.097(0.022)	13.734(0.033)	13.339(0.033)
10	11.928(0.040)	11.416(0.022)	11.093(0.033)	10.778(0.033)

Table 4. MLO Photometric Observations of SN PTF11iqb

UT Date[a]	Day[b]	MJD	B (σ_B)	V (σ_V)	R (σ_R)	I (σ_I)
2011-08-03	11.06	55776.46	...	...	15.049(0.019)	15.031(0.014)
2011-08-06	14.07	55779.47	15.334(0.064)	15.260(0.025)	15.051(0.082)	14.949(0.034)
2011-09-01	39.99	55805.39	...	...	15.619(0.064)	...
2011-09-17	56.02	55821.42	17.036(0.045)	16.447(0.097)	15.902(0.036)	15.623(0.039)
2011-09-23	61.95	55827.35	17.159(0.030)	16.546(0.052)	15.998(0.040)	15.748(0.025)
2011-09-28	67.00	55832.41	17.256(0.069)	16.518(0.042)	15.976(0.035)	15.727(0.033)
2011-10-19	87.91	55853.31	17.582(0.037)	16.877(0.063)	16.160(0.055)	15.985(0.033)
2011-10-27	95.88	55861.28	17.738(0.075)	16.933(0.063)	16.258(0.037)	16.098(0.041)
2011-11-02	101.86	55867.26	17.790(0.058)	17.073(0.041)	16.369(0.046)	16.190(0.027)
2011-11-15	114.89	55880.29	18.130(0.041)	17.525(0.068)	16.717(0.024)	16.546(0.027)
2011-11-18	117.88	55883.28	18.191(0.043)	17.644(0.036)	16.832(0.032)	16.710(0.027)
2011-11-30	129.83	55895.23	18.599(0.034)	18.485(0.023)	17.533(0.026)	17.719(0.031)

Note: All photometric observations were made with the Mount Laguna Observatory 40-inch telescope.
[a]yyyy-mm-dd.
[b]Days since first detection, 2011-07-22.9 UT (MJD 2,455,765.4).

transformation error by taking the standard deviation of the spread of the standard magnitudes obtained using each of the local standard stars. The photometric and transformation errors were then added in quadrature to obtain the uncertainty reported in Table 4; in nearly every case, the total error was dominated by the uncertainty in the transformation.

2.4 Swift/UVOT Ultraviolet Photometry

The Ultra-Violet Optical Telescope (UVOT; Roming et al. 2005) onboard *Swift* observed PTF11iqb in the $UVW1$, $UVM2$, and $UVW2$ filters beginning on 2011 July 24. We photometered the UVOT data using standard procedures within the HEASoft[4] environment. We used a $3''$ diameter aperture to extract flux from the transient, and subtracted coincidence-loss-corrected count rates from underlying host emission obtained from images in 2014 (e.g., Brown et al. 2009). Photometric calibration was performed using the recipes from Poole et al. (2008). The resulting magnitudes, all corrected to the AB system, are displayed in Table 5.

2.5 Spectroscopy

PTF11iqb was brightening quickly at the time of discovery and was presumably caught very early after explosion (see below), so we quickly initiated spectroscopic follow-up observations starting on day 2 after first detection (1 day after discovery). We obtained several epochs of optical spectroscopy of PTF11iqb, which were densely sampled at early times (see Fig. 3, where epochs of spectroscopic observations are plotted above the light curve). We obtained spectra of PTF11iqb using a number of different facilities, including the Bluechannel (BC) spectrograph on the 6.5-m Multiple Mirror Telescope (MMT), the Multi-Object Double Spectrograph (MODS; Byard & O'Brien 2000) on the LBT, the Double Beam Spectrograph (DBSP; Oke & Gunn 1982) on the Palomar 200-inch telescope (P200), the Intermediate dispersion Spectrograph and Imaging System (ISIS[5]) on the 4.2-m William Herschel Telescope (WHT), GMOS on Gemini South, the Kast spectrograph (Miller & Stone 1993) on the Lick 3-m Shane reflector, the Low-Resolution Imaging Spectrometer (LRIS; Oke et al. 1995) mounted on the 10-m Keck I telescope, and the Deep Imaging Multi-Object Spectrograph (DEIMOS; Faber et al. 2003) on Keck II. Details of the spectral observations are summarised in Table 6, and the spectra will be released on the Weizmann Interactive Supernova Data Repository (WISeREP; Yaron & Gal-Yam 2012; `http://www.weizmann.ac.il/astrophysics/wiserep/`).
The slit was always oriented at the parallactic angle (Filippenko 1982), and the long-slit spectra were reduced using standard procedures. Final spectra are shown in Figure 4, although a few epochs of spectra are not displayed in this figure because they were taken close in time to another spectrum that appears very similar. The earlier

[4] `http://heasarc.nasa.gov/lheasoft/`

[5] http://www.ing.iac.es/PR/wht_info/whtisis.html

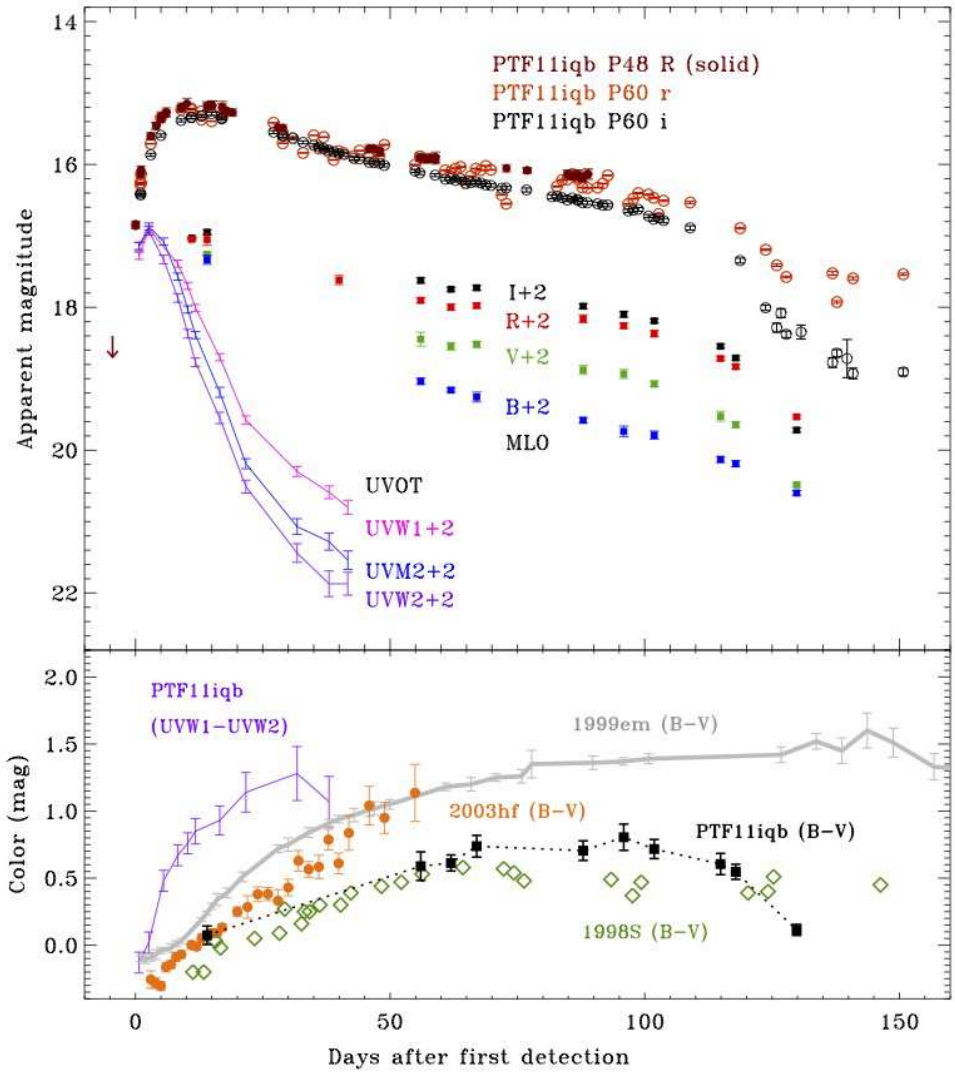

Figure 2. *Top:* Apparent magnitudes for the early part of the light curve for PTF11iqb, with P48 R-band in solid red dots, and with P60 r' and i' bands shown with unfilled circles in red-orange and black, respectively (see Tables 1 and 2). *Swift*/UVOT ultraviolet photometry in the UW1, UM2, and UW2 filters is shown in magenta, blue, and purple, respectively (see Table 5). UVOT magnitudes are offset by +2 for clarity. $BVRI$ photometry from Mount Laguna Observatory (MLO) is shown in blue, green, red, and black squares (Table 4), with all four MLO bands offset by +2 mag for clarity. These are all observed apparent magnitudes (i.e., not corrected for Milky Way reddening). *Bottom:* Colour evolution of PTF11iqb in the UV (UVW1–UVW2; purple) and visible wavelengths ($B-V$; black squares). For comparison, $B-V$ colours for the SN II-P SN 1999em (thick grey line; Leonard et al. 2002), SN II-L 2003hf (orange circles; from Faran et al. 2014), and the SN IIn SN 1998S (green diamonds; Fassia et al. 2000) are shown.

Table 5. Swift/UVOT photometry of PTF11iqb

MJD	UM2 (mag)	σ (mag)	UW1 (mag)	σ (mag)	UW2 (mag)	σ (mag)
55766.1	15.14	0.05	15.28	0.05	15.15	0.06
55768.0	14.87	0.05	14.91	0.05	14.93	0.06
55770.9	15.08	0.05	...	...	15.33	0.06
55773.7	15.57	0.05	15.39	0.05	15.87	0.06
55775.6	16.03	0.05	15.70	0.05	16.37	0.06
55777.2	16.39	0.05	16.01	0.05	16.77	0.06
55781.9	17.19	0.07	16.70	0.05	17.55	0.08
55787.1	18.19	0.07	17.58	0.06	18.51	0.09
55797.1	19.07	0.11	18.30	0.07	19.44	0.13
55803.4	19.28	0.12	18.59	0.09	19.87	0.18
55807.1	19.54	0.13	18.80	0.10	19.87	0.16

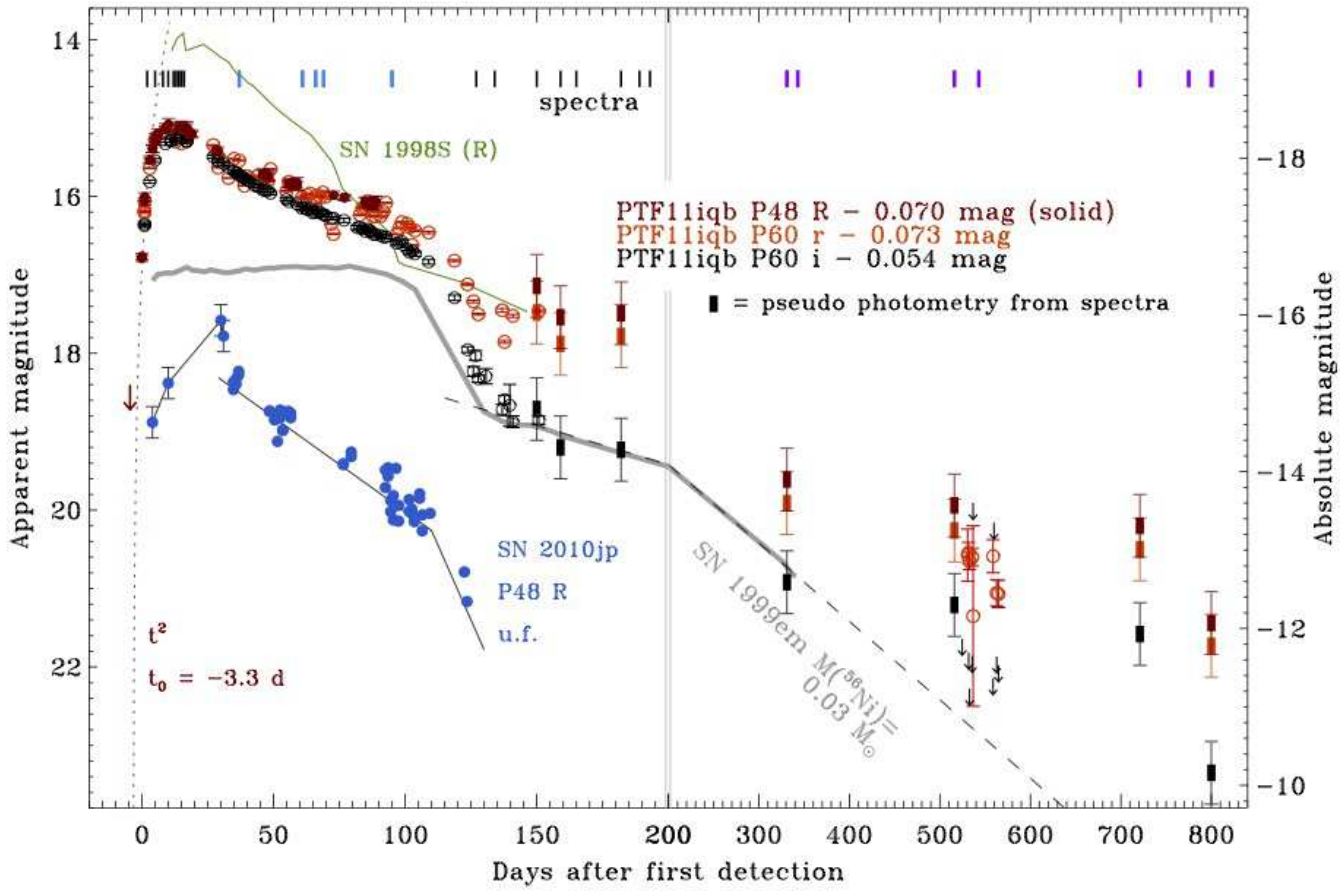

Figure 3. Apparent and absolute magnitude light curve for PTF11iqb, with P48 R in solid red dots, and with P60 r' and i' shown with unfilled circles in red-orange and black, respectively (see Tables 1 and 2). The arrows at late times are P60 upper limits, whereas the solid rectangles at late times (after day $\sim$ 150) represent pseudo-photometry estimated from spectra as described in the text. All photometry for PTF11iqb in the three filters has been corrected for Milky Way reddening of 0.070, 0.073, and 0.054 mag, for R, r', and i', respectively. Epochs when we obtained visual-wavelength spectra are noted with coloured hash-marks at the top (see Table 3 and Figure 4). For reference, we also show R-band light curves of the normal SN II-P 1999em (Leonard et al. 2002), the unusual SN IIn 2010jp (Smith et al. 2012), and SN 1998S (Fassia et al. 2000), scaled as they would appear if they were at the same distance as PTF11iqb. The dashed line is representative of the ^{56}Co decay rate, matched to SN 1999em. Note that the time axis is not uniform; we include a change in scale at 200 days to better facilitate the display of the early-time plateau phase on the same plot as the more sparsely sampled late-time decay.

epochs in Figure 4 have a blackbody plotted in grey for each observed spectrum; these correspond to the temperatures listed as $T_{\rm BB}$ in Table 6, although these are intended only as a rough relative comparison because they depend on the adopted reddening. Nevertheless, inferred temperatures around 7000 K in the plateau phase suggest that these quoted temperatures are not wildly in error. Details of the Hα line profile are shown in Figure 5.

Since our P48 and P60 photometry covers early times well, but includes poor sampling after day 150 (and only upper limits in the i' band on days 500–600), we supplement our imaging photometry by using our flux-calibrated spectra. In spectra taken after day 150, we measured integrated fluxes within specific wavelength ranges to simulate the flux that would be observed in the R (5700–7300 Å), r' (5500–6700 Å), and i' (6900–8100 Å) filters, and then converted these fluxes to magnitudes and added them to Figure 3 as solid rectangles with the same symbol colours as the imaging photometry. The uncertainty here is difficult to quantify, since the main source of error is the exact positioning of the target and associated standard star within the slit, but we adopt representative errors of $\pm$0.4 mag in Figure 3 (at earlier times when our photometry overlaps with spectra, the spectrophotometry generally agree to 0.4 magor better). As discussed in more detail below, it is important to recognise that at the redshift of PTF11iqb, the main difference between the R and r' filters is that R includes the full Hα emission-line profile, whereas the red end of the r' filter cuts off the red wing of PTF11iqb's Hα line. It is also important to note that the pseudo-photometry from spectra subtracts the background by sampling host-galaxy light on either side of the SN, whereas the imaging photometry utilises background subtraction with a SN-free reference image. Thus, if there is an underlying star cluster or other coincident source, it will be included in the spectral photometry but will be absent in the imaging photometry. This may be important at late times when PTF11iqb is faint, so the true brightness of PTF11iqb may be below the level indicated by the spec-

Table 6. Spectroscopic Observations of PTF11iqb

Date	Tel./Instr	Day	$\Delta\lambda$(Å)	$T_{\rm BB}$(K)
2011 Jul 24	GS/GMOS	2	3500–7400	25,000
2011 Jul 24	P200/DBSP	2	3520–9825	25,000
2011 Jul 27	WHT/ISIS	5	3500–9500	16,000
2011 Jul 30	WHT/ISIS	8	3500–9500	...
2011 Aug 01	Keck2/DEIMOS	10	5150–7800	...
2011 Aug 04	Lick/Kast	13	3436–9920	10,500
2011 Aug 05	Lick/Kast	14	3436–9920	10,500
2011 Aug 06	P200/DBSP	15	3520–9825	10,000
2011 Aug 07	WHT/ISIS	16	3500–9500	10,000
2011 Aug 28	P200/DBSP	37	3520–9825	6,500
2011 Sep 21	P200/DBSP	61	3520–9825	6,500
2011 Sep 26	Keck1/LRIS	66	3200–7350	...
2011 Sep 29	Keck2/DEIMOS	69	4500–9300	6,500
2011 Oct 25	Lick/Kast	95	3436–9920	5,600
2011 Nov 26	Keck1/LRIS	127	3340–10300	7,500
2011 Nov 26	Lick/Kast	127	3436–9920	7,500
2011 Dec 02	Keck1/LRIS	134	3300–7400	7,500
2011 Dec 18	Lick/Kast	150	3436–9920	7,500
2011 Dec 27	Lick/Kast	159	3436–9920	7,500
2012 Jan 02	MMT/BC	165	5550–7500	...
2012 Jan 19	MMT/BC	182	3820–9000	7,500
2012 Jan 26	Bok/SPOL	189	3900–7600	7,500
2012 Jan 30	MMT/BC	193	5550–7500	...
2012 Jun 16	Keck1/LRIS	331	3330–10100	...
2012 Jun 28	MMT/BC	343	5550–7500	...
2012 Dec 18	Keck1/LRIS	516	3400–10200	...
2013 Jan 14	MMT/BC	543	5550–7500	...
2013 Jul 11	Keck2/DEIMOS	721	4400–9600	...
2013 Sep 04	MMT/BC	775	nondetect.	...
2013 Sep 29	LBT/MODS	801	5500–10000	...
2014 Jul 29	Keck/LRIS	1104	3400–10200	...

trophotometry. Nevertheless, these measurements provide a useful guide for the late-time evolution.

3 RESULTS

3.1 Light Curve

The multiband light curves and colour evolution for the early phases of PTF11iqb are shown in Figure 2, while Figure 3 shows a subset of the data on an absolute-magnitude scale and extended to later times, as compared to a few previously observed SNe. The light curve displays a rapid rise in only $\sim$ 10 days to a peak luminosity of about -18.4 mag. This is followed by a decline that flattens out in a plateau or shoulder at about -17 mag, dropping off the plateau after 100–120 days.

To the extent that flux proportional to t^2 is a valid description of the early rise, the dotted curve in Figure 3 suggests that explosion occurred at roughly -3.3 days (i.e., 3.3 days before day 0, defined here as the first detection on 2011 July 22.37). This is consistent with the upper limit of 18.5 mag (unfiltered) for our nondetection on 2011 July 17.47 (Parrent et al. 2011), indicated by the red arrow in Figure 3. Since this upper limit corresponds to an absolute magnitude of around -15 mag, it does not place strong constraints on the luminosity or duration of a possible pre-SN eruption. The relatively quick rise to peak in only a few days seems to suggest an extended progenitor star similar to a RSG, which is a topic we discuss in more detail later.

The visible-wavelength colour evolution of PTF11iqb (see Figure 2) starts out very blue and becomes steadily redder for the first 60–70 days, and then seems to level off at $B-V \approx 0.75$ mag before becoming more blue again at late times. PTF11iqb never gets as red as a normal SN II-P, like SN 1999em, probably owing to the continued influence of CSM interaction. The $B-V$ colour evolution of PTF11iqb is quite similar to that of SN 1998S, although at early times it is also similar to a Type II-L event like SN 2003hf (the photometry here is from the recent study of SNe II-L by Faran et al. 2014). We demonstrate later that the spectra around days 30–60 most closely resemble SNe II-L at similar times. The UV colours are very blue at early times, but quickly redden as the UV luminosity plummets and the photosphere cools rapidly in the first 30–40 days after explosion.

There is little change in colour or luminosity during the latter part of the plateau phase from days $\sim$ 50 to

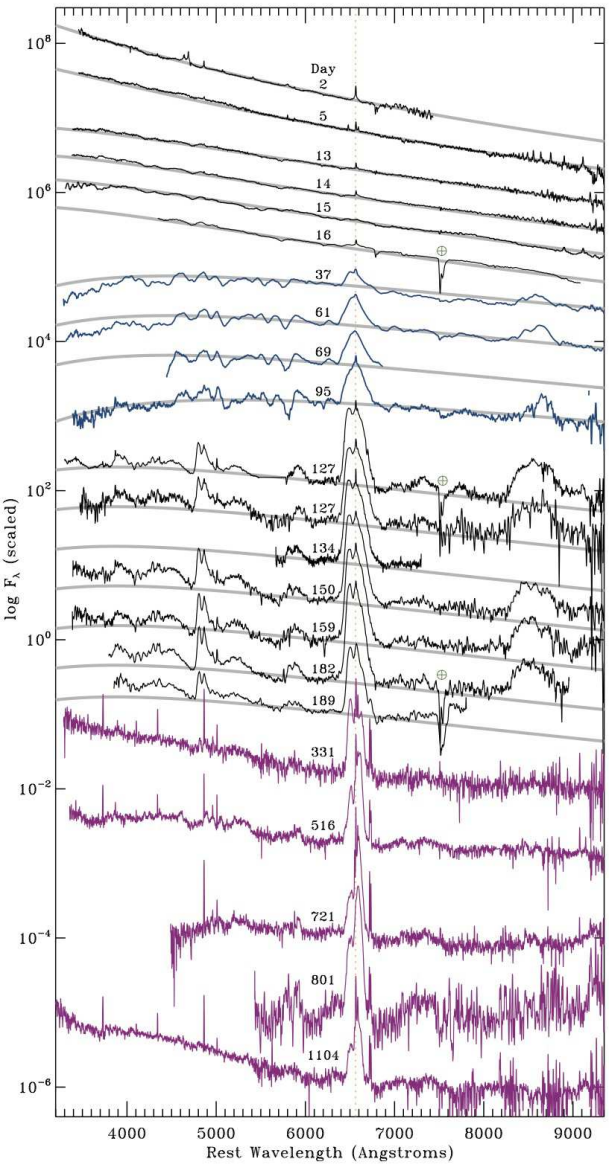

Figure 4. Low/moderate resolution spectra of PTF11iqb (see Table 6), with early times at the top and later times at the bottom. The four main phases discussed in the text are marked with changing colours: early times with CSM interaction (black), the plateau (blue), the early nebular phase (black), and the late nebular phase dominated again by CSM interaction (magenta). Strong telluric features are marked with "$\oplus$".

120. After the drop from this plateau, PTF11iqb exhibits a nebular phase that (at least in the i' band) roughly follows the luminosity decline expected for radioactive decay from ^{56}Co (see Figure 3). While PTF11iqb is qualitatively similar to the light-curve behaviour of SNe IIn-P in this respect (Mauerhan et al. 2013b; Smith 2013b), the drop after the plateau was not nearly as severe, and the late-time radioactive-decay luminosity was not as low. Also, as we discuss below, during the decline from peak and the plateau phase, the spectrum does not show a strong Type IIn signature (resembling SNe 1994W and 2011ht), but more closely resembles spectra of SNe II-P and II-L. Thus, its spectral evolution was unlike the rather homogeneous class of SNe IIn-P (Mauerhan et al. 2013b), which exhibit a persistent SN IIn spectrum throughout their evolution. For these reasons we do not classify PTF11iqb as a Type IIn-P event, although we acknowledge that SN classification criteria may be inadequate if an object morphs through different types as it evolves.

Based on an analysis of the spectra (below), it is clear that the i' band traces the true continuum luminosity much better than the R or r' bands. After the drop of the plateau in the light curve at 100–120 days, the red filters are dominated by strong Hα emission from CSM interaction, to a different degree in each filter because of their different wavelength responses (see above). The i' band does not include the bright Hα line. From the time of the plateau drop until about day 500, the i' band is consistent with radioactive decay from ^{56}Co, and in fact has about the same luminosity and decline rate as the prototypical Type II-P SN 1999em. This would imply a synthesised ^{56}Ni mass of roughly $0.03\,M_\odot$ (for SN 1999em, this was estimated as $0.02\,M_\odot$ by Elmhamdi et al. 2003 and $0.036\,M_\odot$ by Utrobin 2007), and hence, a normal core-collapse SN II-P.

As discussed later, we attribute the excess luminosity (compared to SN 1999em) in the first half of the plateau to CSM interaction, as well as the strong late-time Hα emission. At the very latest phases (after day 500) the true underlying continuum level is very uncertain, since photometry from template-subtracted images only provides upper limits, whereas the pseudo-photometry estimated from spectra does not correct for a possible underlying star cluster or other faint coincident source, and may therefore be an overestimate of PTF11iqb's luminosity by an amount that is difficult to quantify.

3.2 Spectral Evolution

Here we provide a brief overview of the main stages in the spectral evolution of PTF11iqb. The spectra are discussed in more detail below in the comparison with SN 1998S, as well as in sections discussing the late-time Hα and early-time WR features specifically. We highlight three main stages: (1) at very early times around peak luminosity, (2) days 20–100, corresponding to the latter part of the plateau in the light curve, and (3) during the nebular phase after day ~ 120.

3.2.1 Early Spectral Evolution

For the first $\lesssim$ 20 days after explosion, the spectrum of PTF11iqb was characterised by a smooth blue continuum matched by a blackbody that cools quickly from about $\gtrsim$25,000 K on day 2 to about 10,000 K on day 16. The spectrum on day 2 shows a narrow (unresolved at FWHM $\approx$ 500 km s^{-1} at this epoch) Hα line core with broader and symmetric Lorentzian wings extending to about $\pm$2000 km s^{-1}, and also shows a comparably strong "Wolf-Rayet" emission feature (a combination of He II λ4686 and C III/N III). By day 5 these features have mostly faded; thereafter, only narrow Balmer lines remain atop the smooth blue continuum. Similar WR features have been seen in a few other SNe at early times; this is discussed more in §7.

3.2.2 Plateau Spectral Evolution

Starting on day 16, we begin to see an underlying broad component of Hα that continues to grow in strength as the narrow component fades (Figures 4 and 5a). This broad component arises in the underlying fast SN ejecta. There is some persistent very faint narrow Hα emission during the plateau phase, but it is difficult to ascertain how much of it may be contributed by underlying H II regions, since its strength varies from one spectral epoch to the next (which could be caused by true intensity changes, or by various amounts of surrounding H II region emission being included in the slit). In any case, the narrow component of Hα is faint (a few percent of the total Hα flux). On the other hand, the radius of the CSM interaction front in our model (see below) and the SN ejecta photospheric radius are comparable at this epoch, so perhaps the CSM interaction intensity remains steady, but much of the shock interaction region is overtaken by the opaque SN ejecta photosphere (see below).

After about a month, the featureless hot blue continuum from the earlier phase transforms into a spectrum dominated by broad absorption and emission profiles, as in normal ejecta-dominated SNe like SNe II-L and II-P. Besides the broad Hα line with a width of $\sim$10,000 km s^{-1} (FWZI), we see numerous absorption features in the blue typical of SNe II-P (Dessart et al. 2013), as well as the broad Ca II near-infrared (IR) triplet in emission. Some of the absorption (especially Hα and Ca II) appears muted compared to canonical SN II-P atmospheres. Indeed, PTF11iqb's relatively weak P-Cygni absorption in Hα and Ca II more closely resembles that of SNe II-L than SNe II-P, while at 4000–6000 Å, SNe II-P and II-L look qualitatively very similar (see Figure 6). Gutiérrez et al. (2014) discuss the diversity in the ratio of Hα absorption to emission (a/e) in SNe II-P and II-L, and PTF11iqb resembles objects in that study with lower a/e vaues. So overall, even though the light curve shows a clear underlying plateau, the spectrum during the plateau phase looks more like that of SNe II-L; we suspect that this may be due to reionisation of the outer SN ejecta by CSM interaction. As we discuss below, the SN II-L-like spectral appearance is shared by SN 1998S at similar times in its evolution.

3.2.3 Late-Time Spectral Evolution

After the drop in luminosity at the end of the plateau (after days 100–120), the Hα emission from PTF11iqb starts to become quite interesting, exhibiting an asymmetric and multipeaked profile (Figure 5b). During this stage, Hα develops a strong and somewhat broad blueshifted emission peak

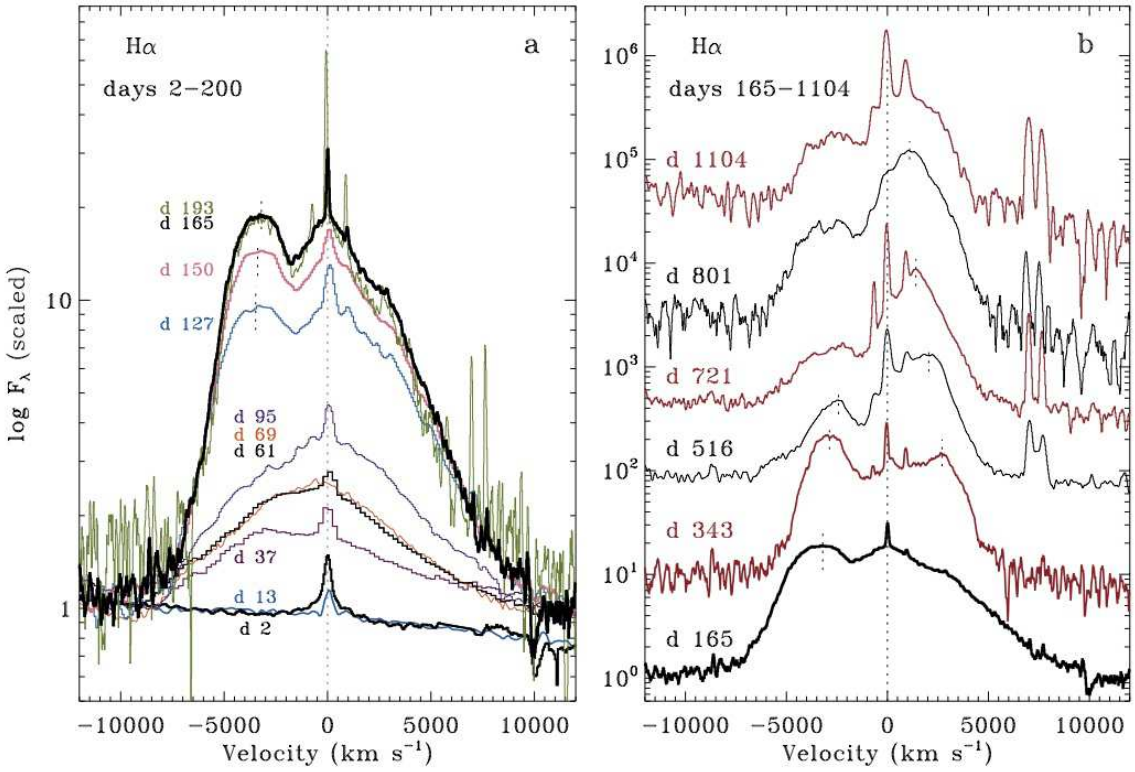

Figure 5. Details of the Hα line profile of PTF11iqb. (a) The left panel shows relatively early-time data, from the time of discovery until the beginning of the nebular phase. These spectra are normalised to the continuum level, and the time sequence of line strength (including broad components) leads to spectra that generally go up with time on this plot. (b) The right panel shows late-time spectra during the nebular phase from days 165 onward. Short vertical lines (dotted) mark velocities measured for relatively well-defined red and blue peaks (see text and Figure 8).

centered at −3000 to −3500 km s^{-1}. The red side of the line shows no similar peak, but instead begins to drop off sharply at around +3000 km s^{-1}. This asymmetric blueshifted Hα profile changes little over the time period from days 120 to 200 (Figure 5a).

Blaming this strong blueshifted asymmetry of Hα on dust or opaque SN ejecta (blocking the receding side) would seem appealing, were it not for the fact that the asymmetric Hα profile then transitions from a blueshifted asymmetry to a much stronger *redshifted* peak between days 331 and 516 (Figure 5b). In the day 516 spectrum and afterward, the red peak of Hα remains stronger than the blue peak (even if dust that was previously blocking the red side were destroyed, it would not make the red side brighter; true asymmetry in the CSM density is needed). We note that a delay in light-crossing time from the back to the front of the SN cannot explain this shift from blue to red peaks, since the light-crossing time is less than 10 days at radii of $\sim$ 500 AU.

Interestingly, the strength of the blueshifted peak coincides temporally with a lingering blue continuum and broad SN ejecta lines like the Ca II IR triplet. These are strong in the early phases of the nebular decay, as in typical SNe II-P. From day 516 onward, however, the blueshifted peak of Hα, the blue continuum, and the broad ejecta lines all fade in tandem. When the red peak is strongest (after day 500), the overall spectrum is dominated by Hα with very little continuum contributing to the observed spectrum. This probably signifies that the spectrum at days 120–200 has a substantial contribution from the normal radioactivity-powered nebular emission from the inner ejecta, and this is when the *i*-band light curve and the Hα line luminosity (see below) both follow the ^{56}Co decay rate. At the latest times (after 300–500 days), the spectrum is dominated by CSM interaction because the radioactivity has faded much faster than the ongoing CSM interaction luminosity.

A narrow emission component of Hα is seen at several epochs, most likely tracing the preshock CSM. Our highest-resolution spectra are those epochs obtained at late times with the MMT using the 1200 line mm^{-1} grating, which are most suitable to constrain the preshock wind speed. Examining epochs that appear to have less contamination from surrounding H II regions (days 37, 61, 69, 95, 127, 150, 165; probably owing to better seeing, evidenced by weaker [N II] emission adjacent to Hα), we find that the narrow component of Hα has Gaussian FWHM values of $\sim$ 80 km s^{-1}, comparable to the spectral resolution of the data. The preshock wind is therefore much slower than that of a typical WR star ($\sim 10^3$ km s^{-1} or more), or that of a blue supergiant or luminous blue variable (LBV; 100–500 km s^{-1}), and closer to values seen in cool red or yellow supergiants (YSGs; see Smith 2014). We quote 100 km s^{-1} as a fiducial value for the CSM expansion speed below, but the actual wind speed and mass-loss rates may be smaller by a factor of 2–3.

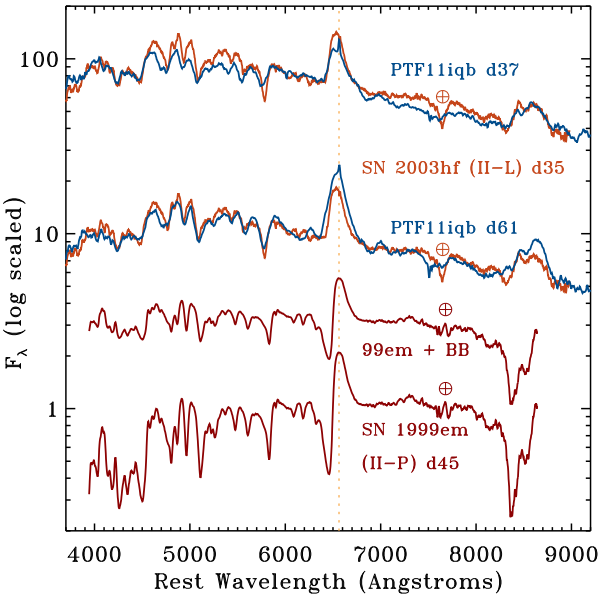

Figure 6. Comparison of visible-wavelength spectra of PTF11iqb on days 37 and 61 (blue) with those of SNe II-L (SN 2003hf; orange) and II-P (SN 1999em; red). For SN 1999em, we show the observed day 45 spectrum, as well as that same spectrum added to a blackbody to dilute the strength of absorption features. These spectra of SNe 2003hf and 1999em were obtained from the UC Berkeley SN database, and appeared in Faran et al. (2014) and Leonard et al. (2002), respectively.

4 A COMPARISON WITH SN 1998S

Readers familiar with SNe IIn may recognise that our description of the spectral evolution of PTF11iqb in §3.2 sounds remarkably similar to that of the classic well-observed Type IIn object SN 1998S. Figure 7 compares the spectral evolution of the two SNe, with visual-wavelength spectra interleaved in chronological order after explosion. The spectra of SN 1998S from Leonard et al. (2000) are taken from the UC Berkeley SN database (Silverman et al. 2012), and the others are downloaded from the WISeREP (Yaron & Gal-Yam 2012) database, originating from papers by Fassia et al. (2001) and Pozzo et al. (2004). The days listed in Figure 7 are relative to discovery as noted by those authors; the explosion date of SN 1998S is not known precisely, but may be a few days before discovery (Leonard et al. 2000).

Basically, the spectra of the two SNe in Figure 7 are almost identical in their evolution, sufficient to claim that PTF11iqb is a near twin of SN 1998S. Both SNe proceed through all the same spectral changes outlined above at roughly similar times. We note two exceptions to this twinhood.

First, spectral signatures of CSM interaction are generally stronger in SN 1998S at early times, consistent with its significantly higher peak luminosity (Figure 3). In its day 2 spectrum, PTF11iqb shows an almost identical broad-winged Lorentzian Hα profile and Wolf-Rayet (WR) features to those that were first described in detail for SN 1998S by Leonard et al. (2000). Chugai (2001) noted how these can arise from CSM interaction in the opaque inner wind. An alternative explanation for the early-time spectrum may

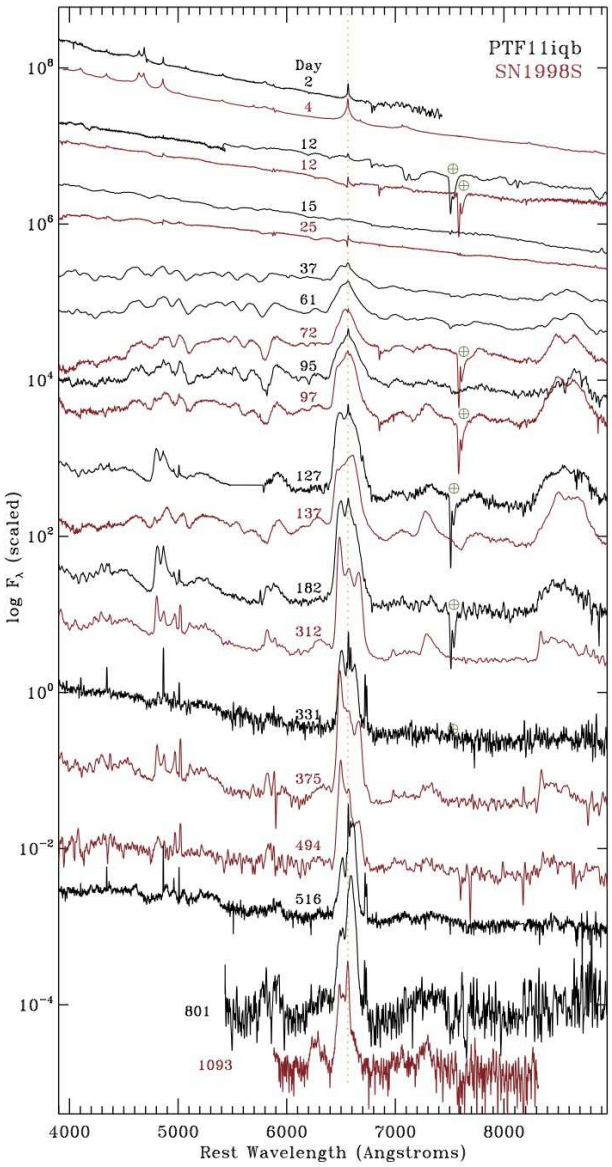

Figure 7. The spectral evolution of PTF11iqb compared to that of SN 1998S. All spectra of PTF11iqb are black, and all spectra of SN 1998S are red. Spectra of PTF11iqb for various epochs are the same as in Figure 4. Spectra of SN 1998S are from Leonard et al. (2000) (days 4, 25, 137, 312, 375, and 494), Fassia et al. (2001) (days 12, 72, and 97), and Pozzo et al. (2004) (day 1093). The days for SN 1998S are as listed by those authors; this could cause offsets of a few days compared to PTF11iqb, which may be relevant at early times when comparing the two SNe, but which will not be significant at later times.

be ionisation of a dense inner wind by a UV flash from shock breakout, as was hypothesised to occur in SN 2013cu (Gal-Yam et al. 2014). It is difficult to distinguish between these two hypotheses with the available data, but in either case, PTF11iqb requires an opaque inner wind at a radius of ~ 10 AU. An argument in favour of CSM interaction being important is that the wind density parameter required for the inner wind is very similar to that in the outer wind required by the late-time CSM interaction when the emission is optically thin (see §7). In any case, the key difference as

compared to SN 1998S is that in PTF11iqb these features are weaker and they fade more quickly. In the day 2 spectrum of PTF11iqb, we measure EW(Hα) = 13.5 $\pm$ 0.8 Å and EW(WR) = 29.6 $\pm$ 1.0 Å (emission-line EWs are positive). The WR bump and strong Lorentzian wings of Hα are only seen in the day 2 spectrum and they fade completely by day 5 in PTF11iqb, leaving only a narrow Hα component. In SN 1998S, by contrast, these features are still quite strong in the days 3, 4, and 5 spectra shown by Leonard et al. (2000). In the day 4 spectrum of SN 1998S in Figure 7, we measure EW(Hα) = 55$\pm$1.0 Å and EW(WR) = 39$\pm$1.0 Å. Note that because of the higher luminosity of SN 1998S, the line luminosities are about an order of magnitude larger in SN 1998S. It is also interesting to note that the EW(WR)/EW(Hα) ratio is higher in PTF11iqb, perhaps reflecting the fact that the spectrum was obtained sooner after explosion than for SN 1998S, or perhaps higher ionization at lower densities.

Second, PTF11iqb shows an interesting and significant difference in its late-time Hα profile evolution. Both objects exhibit qualitatively similar asymmetric and multipeaked Hα lines at late times. However, PTF11iqb shifts from having a prominent blue peak at days 120–200 to a very strong red peak after day 500. SN 1998S does not do this, and stays with a blue peak continually. This is significant because the persistent blue peak of SN 1998S at late times was attributed to dust formation blocking the receding parts of the system (Leonard et al. 2000; Pozzo et al. 2004). The nearly identical temporal evolution of PTF11iqb, but with the difference of ending with a stronger redshifted peak, implies that this asymmetry may be caused by nonaxisymmetric structure and viewing orientation, rather than preferential extinction of the far side by dust. The asymmetry in the CSM is discussed more below (see §6).

Aside from these two points, the spectra of PTF11iqb and SN 1998S are basically the same. How does this fit with their light curves? SN 1998S was roughly a factor of 4 more luminous at peak, consistent with stronger CSM interaction, whereas the two had very similar luminosities from about day 80 onward. In the next section, we show that we can approximate the light curve of PTF11iqb by adding the luminosity from weak[6] CSM interaction to the light curve of a normal SN II-P. This veils the sharp drop in a normal plateau, making it a more gradual "shoulder" in the light curve. If we crank up the early-time CSM interaction in this scenario, the peak luminosity will be higher, and the shoulder in the light curve owing to the underlying SN II-P plateau will be harder to recognise, resembling SN 1998S. Thus, the inference that PTF11iqb was like SN 1998S but with weaker CSM interaction seems qualitatively consistent with both the spectra and light curves.

5 A MODEL LIGHT CURVE

In Figure 8 we demonstrate that one can approximately match the light curve of PTF11iqb using a SN II-P light curve that has extra luminosity from CSM interaction added to it. The SN II-P light curve we adopt is that of SN 1999em (Leonard et al. 2002), but of course this is just a convenient reference. (We could have used a different SN II-P with a somewhat different light curve, and then adjusted the CSM parameters accordingly.) To this we add luminosity from CSM interaction ($L_{\rm CDS}$; the luminosity of the cold dense shell), calculated from a simple model with fast SN ejecta overtaking slower dense CSM, and the loss in kinetic energy is converted to radiation (see, e.g., Smith 2013a,b). Models of this type are not unique and have degeneracy in adjustable parameters like explosion energy, CSM mass, CSM radial distribution, and geometry. The model shown here is meant as a plausibility argument that PTF11iqb can be explained with a normal core-collapse SN that has weaker CSM interaction than SN 1998S, and provides only a very rough estimate of the CSM conditions.

Observations of the CDS velocity at late times when the emission is optically thin can help restrict some of the degeneracy in the model. Velocities of the blue and red peaks observed in the late-time Hα profiles are plotted in the bottom panel of Figure 8. Normally, decelerating the fast 10^{51} erg SN ejecta to the observed coasting speed of around 3000 km s^{-1} would require a high CSM mass, and also that roughly half the explosion kinetic energy was radiated away — this would produce a value of $L_{\rm CDS}$ that is much higher than observed in PTF11iqb. To make a CSM-interaction model consistent with the observed velocities without overproducing the luminosity, we must adjust the emergent luminosity by an artificial efficiency factor of $\sim$ 15%. One option to accomplish this physically is to simply lower the CSM density and the SN ejecta mass (and SN energy) to 15%. The lower SN ejecta mass and energy would, however, then seem inconsistent with the underlying plateau light curve and radioactive decay tail that indicate a normal SN II-P. A second and simpler option is to interpret the 15% efficiency as a geometric effect — i.e., if the dense CSM only intercepts 15% of the solid angle seen by the SN ejecta, one can still have a normal 10^{51} erg explosion and high-density CSM, but the resulting $L_{\rm CDS}$ is much lower than it would be in a spherically symmetric model with the same parameters. The 15% geometric covering factor could, in principle, arise from CSM that is in a disc or torus, a nonaxisymmetric shell, or clumps that intercept an equivalent fraction of the solid angle.

Agreement between our model and observations does not provide conclusive evidence of asymmetric CSM, but there are a number of reasons why nonspherically symmetric CSM is plausible. First, there is clear observational precedent: the similar explosion SN 1998S was inferred to have a highly aspherical, perhaps disc-like or toroidal CSM based on spectropolarimetry (Leonard et al. 2000). SN 1998S was also inferred to have a disc-like CSM based on the multipeaked asymmetric Hα line profiles seen at late times (Leonard et al. 2000; Gerardy et al. 2000; Fassia et al. 2001; Pozzo et al. 2004), which are very similar to those of PTF11iqb. A flattened CSM geometry was also inferred for the more recent event SN 2009ip based on energetic arguments, spectropolarimetry, and spectral clues (Smith, Mauerhan, & Prieto 2014; Mauerhan et al. 2014; Levesque et al. 2014; Ofek et al. 2013c). Second, our spectra do not exhibit the narrow P-Cygni absorption that one might expect if the required preshock CSM density is along our line of sight to the SN photosphere. Last, evolved massive stars commonly show highly aspherical CSM when their

[6] Here we intend "weak" to mean that CSM interaction is weak enough that it does not dominate the visible wavelength luminosity of the SN ejecta photosphere in these early phases.

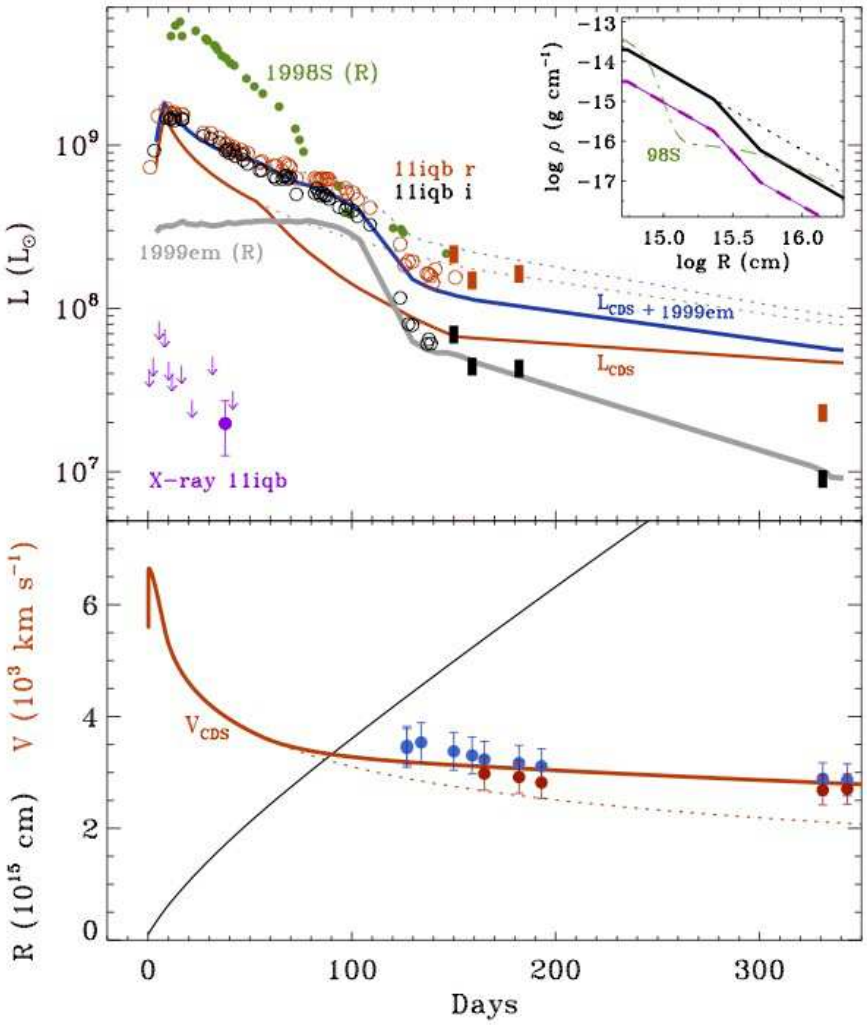

Figure 8. A simple model for the light curve of PTF11iqb. *Top panel:* Luminosities based on the observed r and i-band light curves (red and black data, respectively) of PTF11iqb, compared to a simple model. The thick blue curve that approximates the light-curve shape (labeled $L_{\rm CDS}$+1999em) is a combination of a normal SN II-P light curve (SN 1999em, shown in grey; from Leonard et al. 2002) and a simple CSM interaction model (orange curve labeled $L_{\rm CDS}$). This model results from the radial density distribution shown in the inset at upper right (solid black), but where we have assumed an efficiency of 15% to account for aspherical geometry (see text for details). The dashed purple curve in this panel is the equivalent density distribution with the same mass if the model were spherically symmetric. The dashed green curve is the radial density distribution from the model for SN 1998S by Chugai (2001). In the luminosity plot (top), the dotted blue and dotted red/orange curves show what the total luminosity would look like with a constant wind density parameter w, corresponding to the dotted black line in the radial density plot. (The R-band light curve of SN 1998S from Fassia et al. (2000) is shown for comparison, as are X-ray data for PTF11iqb from Ofek et al. (2013b)). *Bottom panel:* The evolution of the cold dense shell (CDS) radius (black) and velocity (rust coloured) with time in the CSM interaction model from the top panel. The solid curve labeled $V_{\rm CDS}$ is the velocity for the solid black density distribution in the upper-right inset, and the dotted orange curve corresponds to constant w for comparison. The blue and red data are velocities of the blue and red peaks of the asymmetric Hα line (see Figure 5).

nebulae are spatially resolved (this is discussed more in the next section).

A substantial fraction of $L_{\rm CDS}$ in our model should escape as X-rays rather than being converted to visible-wavelength continuum or Hα emission. Although the observed X-ray luminosity at early times shows that only a small fraction of the X-ray luminosity escapes (Figure 8 and Ofek et al. 2013b), there have not yet been published constraints for late-time X-ray emission from PTF11iqb. This is expected theoretically for most SNe IIn (Chevalier & Irwin 2012; Svirski et al. 2012). From our analysis of the late-time Hα (see below) we infer that the wind density parameter in the outer wind may actually be similar to that in the very inner wind, arguing that the drop in density at $10^{15.5}$ cm used to model the light curve merely reflects a decreasing optical depth of the outer wind and larger escape fraction of X-rays. As the material expands to larger radii and the optical depth drops, we would indeed expect a larger fraction of the total postshock luminosity to escape as X-rays (moreso if the geometry is not spherically symmetric). This would occur after the plateau.

The model that matches the observed light curve best

in Figure 8 is qualitatively very similar to the model for SN 1998S presented by Chugai (2001), with a higher density inner wind transitioning to a lower density outer wind (again, this drop may merely reflect a larger escape fraction of X-rays at lower optical depth or a different geometric covering factor; our simple model cannot constrain this further). The radial density profile we adopt is shown by the black line in the upper-right inset of Figure 8. Note, however, that this is the wind density that occupies only 15% of the solid angle, following our assumptions about geometry discussed above. Therefore, this same inset to Figure 8 shows a dashed magenta curve, which is what the model wind density would be if the same mass were averaged over 4π steradians; this is more appropriate when comparing to the spherically symmetric wind density in the model for SN 1998S by Chugai (2001), shown by the green dashed curve in the same inset. So, comparing these one can see that the CSM around PTF11iqb is qualitatively very similar to that of SN 1998S, but with less mass and with a division between the inner and outer wind at $\sim 10^{15.5}$ cm instead of at $\sim 10^{15}$ cm.

Our adopted CSM has an effective (i.e., spherically averaged) wind density parameter ($w \equiv \dot{M}/v_w$) of $w = 10^{15}$ g cm^{-1} for the inner CSM and 2.5×10^{14} g cm^{-1} for the outer CSM. With $\dot{M} = wv_w$, these densities translate to pre-SN mass-loss rates of roughly $1.5 \times 10^{-4}\,M_\odot$ yr^{-1} (inner) and $4 \times 10^{-5}\,M_\odot$ yr^{-1} (outer) for a wind speed of 100 km s^{-1}. The total mass in the inner shell is about $10^{-3}\,M_\odot$ lost in the $\sim$ 8 yr before core collapse, and about $0.04\,M_\odot$ lost in the $\sim$ 1000 yr before core collapse (out to $\sim 3 \times 10^{17}$ cm). These are only order-of-magnitude estimates, owing to possible variation in wind speed, X-ray escape fraction, and geometry. The CSM mass is small compared to the several $M_\odot$ in the massive expanding SN ejecta, but the CSM can be dense enough to resist the expansion of the SN ejecta if it is in a thin disc that intercepts a small fraction of the solid angle of the explosion. These pre-SN mass-loss parameters are less extreme than for other SNe IIn (Kiewe et al. 2012; Svirski et al. 2012; Ofek et al. 2013b), and are within the range of mass-loss rates of several observed classes of moderately massive evolved supergiants (RSGs with dense winds like OH/IR stars, YSGs, B[e] supergiants, and relatively low-luminosity LBVs; see Smith (2014) for a general review of mass-loss rates in evolved massive stars). The CSM for PTF11iqb does not require the most extreme levels of LBV-like eruptive mass loss, but it does imply some significant episodic ejection or wind modulation in the decade before core collapse. Both PTF11iqb and SN 1998S had extended CSM consistent with RSG winds, although on the high end of known mass-loss rates for RSGs (Mauerhan & Smith 2012).

In this model, the total energy radiated by CSM interaction in the first 100 days is at least 10^{49} ergs, although the early rise may be caused partly to shock-breakout luminosity reprocessed by the dense inner wind (see, e.g., Ofek et al. 2010). This is the extra luminosity that is needed in addition to a normal SN II-P light curve. This extra energy can be reduced somewhat if the underlying plateau SN is more luminous (although it can be at most a factor of ~ 1.6 more luminous to not exceed the observed day 80–100 luminosity). The amount of extra radiated energy in only the first 20 days indicated by optical photometry is about 7×10^{48} erg, but this ignores a bolometric correction and so the true radiated energy in this time is probably a factor of several higher, given the high $\gtrsim$25,000 K temperature at the earliest times. In any case, this energy is several times higher than the typical energy of a UV flash associated with shock breakout in a RSG without a dense inner wind.

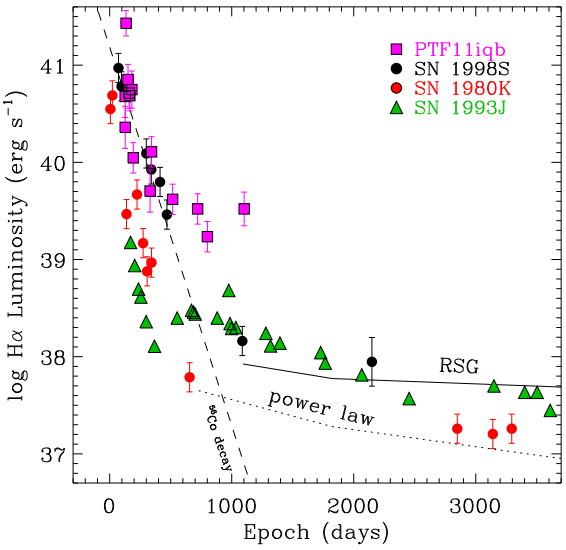

Figure 9. Late-time Hα luminosity of PTF11iqb, as compared to other SNe with strong late-time Hα from CSM interaction. We include SN 1998S and SN 1980K from Figure 4 of Mauerhan & Smith (2012), with SN 1980K Hα data from Milisavljevic et al. (2012). Hα luminosities for SN 1993J are compiled by Chandra et al. (2009).

6 LATE-TIME Hα AND ASYMMETRY

After about 100–120 days, corresponding to the drop in continuum luminosity of the underlying plateau SN light curve, the spectrum of PTF11iqb took on a different character, dominated by a nebular ejecta spectrum plus a very strong Hα line that we attribute largely to CSM interaction. As noted above, the multipeaked Hα line profile is qualitatively very similar to that of SN 1998S (Leonard et al. 2000; Fassia et al. 2001; Pozzo et al. 2004), which was interpreted as arising from CSM interaction in a flattened disc. We note that the late-time Hα from PTF11iqb is also reminiscent of the late Hα emission from the nearby SN IIb explosion SN 1993J (Matheson et al. 2000a,b), where the Hα was also attributed to CSM interaction in an extended disc.

Figure 9 shows the temporal evolution of the integrated Hα line luminosity in PTF11iqb and in a few other SNe with strong late-time Hα.[7] For the first $\sim$ 500 days, PTF11iqb decays at roughly the ^{56}Co rate, and is quite similar to SN 1998S. It is during this time frame that PTF11iqb and SN 1998S both show a strong blueshifted peak in Hα, along

[7] Note that at late times, some of the spectra are contaminated by very narrow nebular Hα and [N II] emission from adjacent H II regions, where variable amounts are present in the spectra owing to seeing differences. We subtracted the contribution of these narrow H II lines from the integrated line flux.

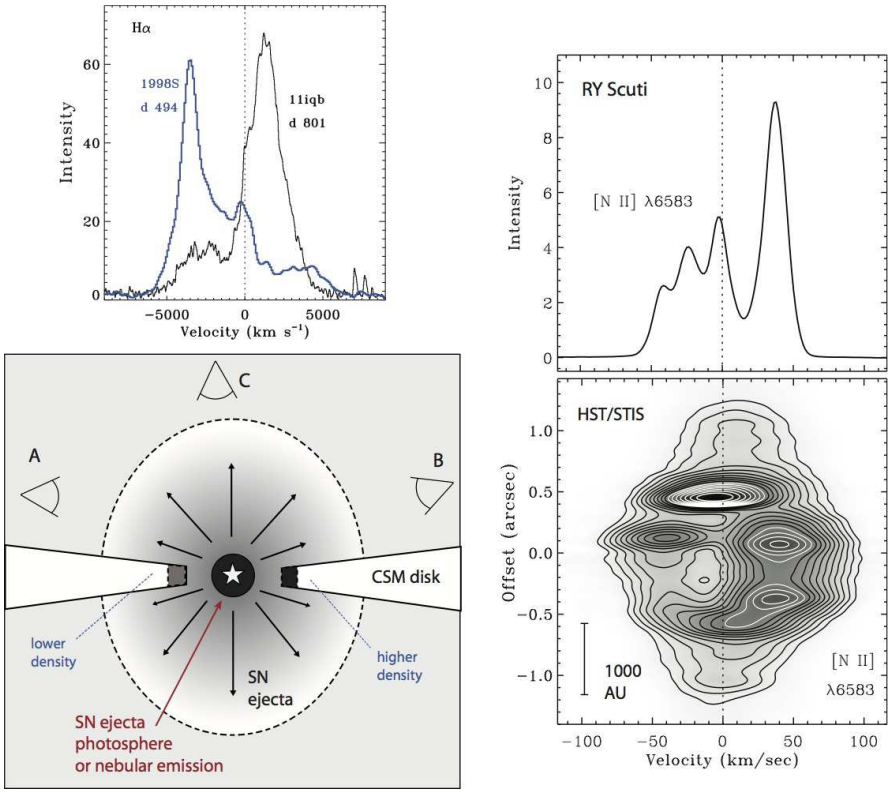

Figure 10. These panels relate to the discussion of asymmetry in §6 of the text. The upper-left plot compares the late-time asymmetric Hα profiles of SN 1998S and PTF11iqb. The lower-left panel is a sketch of CSM interaction for a SN running into a flattened disc-like CSM that has a lower density on the left side and a higher density on the right. A high-inclination observer at position A would see stronger redshifted peaks, as in PTF11iqb, whereas an observer seeing the same event from position B would see a blueshifted peak as in SN 1998S. An observer at low inclination (position C) would see a narrower and more symmetric line profile. The right panels correspond to observations of the torus around the mass-transferring eclipsing binary RY Scuti, from Smith et al. (2002), as seen in [N II] λ6583 emission. The botton panel shows the spatially resolved position-velocity diagram (*HST*/STIS spectra) with the slit aperture running through the major axis of the torus. This reveals an azimuthally asymmetric density distribution around the torus, with higher densities on the receding side. The top-right panel shows the integrated line profile from this circumstellar nebula, seen in a ground-based echelle spectrum. The radius of the torus is about 1000 AU, similar to the CSM encountered by PTF11iqb at late times, and the deduced CSM mass is similar as well. It seems likely that if a SN were to expand into a torus like that around RY Scuti, it would produce CSM interaction signatures much like those observed in PTF11iqb at late times.

with strong nebular lines like the broad Ca II IR triplet. During this time, the Hα luminosity may be powered largely by radioactive decay. As such, the velocity asymmetry in the Hα lines (especially the blue bump), could indicate a highly nonspherical distribution of ^{56}Ni.

After about 500 days, however, the Hα from PTF11iqb decays more slowly than in SN 1998S, SN 1993J, and SN 1980K, and no longer traces the ^{56}Co radioactive-decay rate. During these later times, Hα is therefore most likely powered by CSM interaction. It is during these same later epochs after day 500 when PTF11iqb's Hα profile switches from a blueshifted peak to a stronger redshifted peak. It will be interesting to see how PTF11iqb continues to evolve. In SN 1998S, the drop in Hα luminosity reached a floor at around day 1000, after which it followed a trajectory consistent with CSM interaction in a very dense RSG wind (Mauerhan & Smith 2012), and SN 1980K and SN 1993J behaved similarly (Fesen et al. 1999; Milisavljevic et al. 2012; Matheson et al. 2000b). The stronger day 500–1100 Hα luminosity in PTF11iqb could indicate an earlier onset of this behaviour in a wind that is an order of magnitude more dense (which would be extreme, given that the wind parameters for SN 1998S resembled those of VY CMa, the strongest known RSG wind), or perhaps it is merely overtaking a shell or terminal shock in the RSG wind that temporarily enhances the strength of Hα. Continued observations of PTF11iqb are encouraged. In any case, the fact that PTF11iqb had weaker CSM interaction at early times and stronger interaction at late times compared to SN 1998S suggests that the pre-SN mass loss in SNe IIn does not necessarily follow a common recipe, and that detailed observations of the shock progressing through the distant CSM may help unravel their highly varied mass-loss histories. Most SNe are not observed sufficiently late to see this behaviour, and/or they are too distant. If pre-SN mass loss is punctuated by stochastic mass ejections over a range of timescales, this would be quite relevant for diagnosing the driving mechanism in the final phases before core collapse.

Similarly, if the stochastic mass loss is highly asymmetric (especially azimuthally asymmetric), this may also be an important clue to its underlying physical mechanism. When the asymmetric blueshifted Hα line profiles were seen

at late times in SN 1998S, it was inferred that dust obscuration may have played an important role in making an otherwise more symmetric double-peaked line appear heavily blueshifted (Leonard et al. 2000; Gerardy et al. 2000; Pozzo et al. 2004). Pozzo et al. (2004) mentioned the possibility that dust formed in the postshock region (the CDS) may have been contributing to the asymmetry, as was seen later in the unambiguous case of SN 2006jc (Smith et al. 2008b). However, as noted earlier, we cannot rely upon dust or ejecta obscuration to account for the strong asymmetry seen in PTF11iqb, because this time it is the *blueshifted* material on the near side that is missing. The fact that emission from the far side of the CSM interaction is brighter provides a strict requirement that the density distribution in the CSM is intrinsically asymmetric. Interestingly, the velocity of the brighter red peak is slower (roughly +1100 km s^{-1}) as compared to that of the blue peak (roughly −2000 to −3000 km s^{-1}) on day 801, so stronger deceleration upon running into denser CSM is an intuitively plausible explanation for the brightening of the red side of the line. If SNe IIn typically have such asymmetry, then a range of viewing angles could easily explain why some have redshifted peaks, some have blueshifted peaks, and others have narrower and centrally symmetric Hα profiles at late times, as depicted in the left panels of Figure 10.

What sort of process could produce a flattened CSM geometry that is significantly more dense on one side than the other? Axisymmetric structures in the CSM (discs and bipolar nebulae) may conceivably arise from rapid rotation in single stars, but high degrees of *azimuthal* asymmetry are difficult for single stars to achieve. A way to have one-sided CSM while still satisfying the equatorial mass distribution suggested by spectropolarimetry of SN 1998S is to have mass loss in a binary with some nonzero eccentricity, or with unsteady mass loss. As an illustrative example, the right panels of Figure 10 show observed emission from the nebula around the Galactic massive star RY Scuti. RY Scuti is a rare example of a massive eclipsing binary system caught in the brief phase of mass transfer, where one star is being stripped of its H envelope on its way to the WR phase, and it is so far the only such system known with a spatially resolved toroidal CSM nebula (Grundstrom et al. 2007; Smith et al. 2002, 2011b). Figure 10 shows the spatially resolved velocity structure of the ring and the integrated emission-line profile of [N II] λ6583, from Smith et al. (2002). The integrated line profile from the nebula is multipeaked and very asymmetric, with a brighter red peak — very much like PTF11iqb at late times, but with slower (preshock CSM) expansion speeds of only ±40 km s^{-1}. When emission from RY Scuti's torus is spatially and spectrally resolved (see the position-velocity diagram in the bottom right in Figure 10), it is clear that the density distribution in the expanding torus is azimuthally asymmetric, with several clumps around the torus and generally higher density on the far side (Smith et al. 2002). This azimuthal asymmetry arises despite the fact that the central eclipsing binary system appears to be tidally locked and has a circularised orbit (Grundstrom et al. 2007). In this case, the azimuthal asymmetry may arise from episodic mass loss. Proper motions of the multiple shells around RY Scuti reveal two separate major ejections in the last ∼ 250 yr (Smith et al. 2011b). Such sequential mass-loss episodes in a binary might provide the complex density

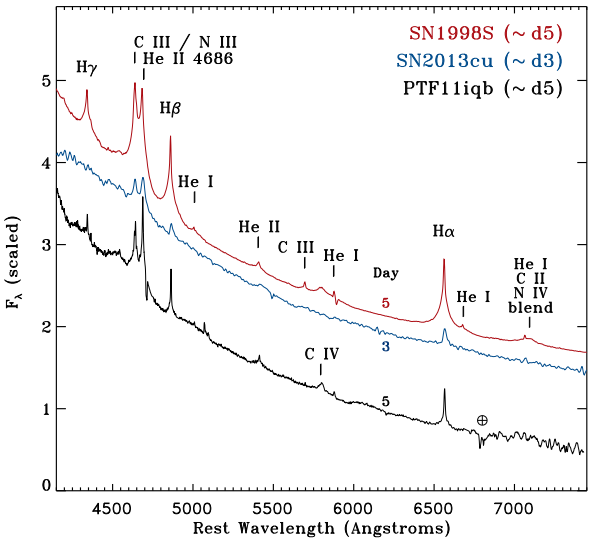

Figure 11. Early-time spectra of PTF11iqb (day 2 after discovery, roughly day 5 after explosion), SN 2013cu (day 3 after discovery and explosion; Gal-Yam et al. 2014), and SN 1998S (day 4 after discovery, day 5 after explosion; Leonard et al. 2000) showing the WR features. The days noted next to each SN name are approximate times after the inferred explosion time. Various lines of highly ionised species such as He I, He II, N III, and C III are seen in the spectra, plus broad Lorentzian wings of Balmer lines. These WR-like features appear despite the likelihood that both the PTF11iqb and SN 1998S progenitors were RSGs, not WR stars, because the dense cool wind becomes highly ionised by shock breakout or CSM interaction from the fastest ejecta.

structure around PTF11iqb; interestingly, the total mass inferred for RY Scuti's nebula of 0.001 M$_\odot$ (Smith et al. 2002) within ∼ 1000 AU is in the right ballpark. We infer that if a Type II-P explosion was surrounded by RY Scuti's nebula, the resulting CSM interaction could produce the late-time Hα emission seen in PTF11iqb. The analogy can only be pushed so far, however, because RY Scuti is a binary of an O star and a B supergiant, so it is unlikely to produce a plateau light curve if it exploded tomorrow. Nevertheless, it provides a nice illustration of the asymmetry that can arise in the CSM around interacting binaries. Many other possibilities exist to create azimuthally asymmetric structure, such as wind collisions or other interactions in binary systems with nonzero eccentricity.

7 WOLF-RAYET FEATURES IN THE EARLY SPECTRUM

PTF11iqb now joins a few other SNe (Types IIn and IIb), which have been caught early and show the WR features associated with He II λ4686 and strong Lorentzian wings of Balmer lines in their very early-time spectra. The best-studied cases of this so far include SN 1998S (Leonard et al. 2000; Chugai 2001) and SN 2013cu (Gal-Yam et al. 2014; Groh 2014). Figure 11 shows these features in detail as they appear in the early spectra of PTF11iqb, SN 1998S, and SN 2013cu. The spectrum of SN 2013cu from Gal-Yam et al. (2014) was obtained from the WISeREP database (Yaron & Gal-Yam 2012).

Recently, Gal-Yam et al. (2014) reported the detection of these same features in the first few days after explosion in SN 2013cu, which was a stripped-envelope Type IIb event. Those authors interpreted the spectral features as resembling a WN6h spectral type. Based on this similarity, Gal-Yam et al. (2014) proposed that the progenitor was a WR-like star. This is an important claim, since no WR progenitors have been detected yet for any stripped-envelope SNe, but relatively cool YSG progenitors have been directly detected in other SNe IIb, the three clear cases being SN 1993J, SN 2011dh, and SN 2013df (Maund & Smartt 2009; Van Dyk et al. 2013, 2014). (Interestingly, SN 1993J behaves very similarly to PTF11iqb and SN 1998S at late times.)

However, in this paper we have shown that these same WR features are seen in PTF11iqb, and they had also been seen previously in SN 1998S.[8] This challenges the WR-like progenitor interpretation forwarded by Gal-Yam et al. (2014), since both PTF11iqb (this work) and SN 1998S (Mauerhan & Smith 2012; Shivvers et al. 2014) have CSM consistent with RSG winds. In the particular case of PTF11iqb, we see a plateau in the light curve, indicating that the underlying SN event was a Type II-P explosion — this requires that the progenitor was an extended cool supergiant at the moment it exploded, and not a compact WR star. From this comparison alone we cannot rule out the possibility that SN 2013cu had a WR-like progenitor, but clearly a WR progenitor is not necessary to yield WR features in a SN. A YSG progenitor, as has been detected directly in other SNe IIb, may provide a suitable alternative for SN 2013cu. Indeed, comparing the spectrum of SN 2013cu to radiative-transfer models, Groh (2014) concludes that the SN 2013cu progenitor could not have been a WR star, and instead must have been a yellow hypergiant (with more extreme mass loss than a normal YSG). The enhancement of N lines in the spectrum that led Gal-Yam et al. (2014) to connect SN 2013cu with a WN star (rather than a WC) star is not exclusive to WR stars, since many cooler evolved massive stars across the upper HR diagram show N-enriched atmospheres (in any case, the strong N lines may be more of a temperature effect than abundance; Groh 2014). Nevertheless, early time data such as the spectra obtained for 2013cu and PTF11iqb provide powerful probes of the immediate pre-SN mass loss (Gal-Yam et al. 2014).

We conclude that the WR-like spectrum seen at early times has little to do with the spectral type of the progenitor before explosion. Instead, it most likely reflects a wind density that is high enough to be optically thick at radii of $\sim$ 10 AU after it becomes ionised.[9] Interestingly, the implied wind density requires a mass-loss rate ($0.001\,M_\odot$ yr^{-1} for SN 2013cu; Groh 2014; Gal-Yam et al. 2014) that is orders of magnitude higher than observed winds of WR stars, and well above the line-driving limit (see Smith 2014); WR stars do not have such high densities at 10 AU because their winds are fast. The required density is more easily achieved in the slow dense winds of cool supergiants (with lower wind speeds, a lower mass-loss rate is required for the same w). Of course, cool supergiants normally lack the ionising photons needed to create the characteristic WR spectrum. A WNH-like spectrum will be produced, however, when any dense cool wind is bathed in a huge flux of hard ionising photons that are capable of fully ionising the wind. The WN features can be strong even when H is abundant in the atmosphere; as a consequence, there are many WNH stars that are not at the same evolutionary stage as He-burning WR stars (see Smith & Conti 2008; Crowther 2007). The requisite blast of hard photons might come from either the UV flash associated with shock breakout (Gal-Yam et al. 2014), or from CSM interaction (Leonard et al. 2000; Chugai 2001) generated when the fastest outer SN ejecta begin to crash into the slow inner CSM. Since this occurs inside the continuum photosphere, it is difficult to know which process dominates, but nevertheless, either process requires a similarly optically thick inner wind.

Lastly, we note that independently, Shivvers et al. (2014) draw a similar conclusion regarding the interpretation of the WR features by Gal-Yam et al. (2014). Shivvers et al. present a high-resolution echelle spectrum of SN 1998S obtained at very early times when the WR emission features were seen in that object. They find a slow wind consistent with a RSG progenitor, and therefore favour a similar interpretation that a WR-like spectrum at early times does not necessarily indicate a WR progenitor.

8 OVERVIEW OF PTF11iqb: BRIDGING TYPE IIn EVENTS WITH NORMAL SNe

In principle, any type of SN explosion could appear as a Type IIn, since the IIn spectroscopic signature is not the result of the explosion physics, but is caused instead by H-rich (or H-poor/He-rich in the case of SNe Ibn) CSM interaction that happens afterward. When CSM interaction is strong, the CSM optical depth is high. Consequently, in cases where CSM interaction substantially enhances the peak visible continuum luminosity of a SN IIn, the photosphere can actually be ahead of the forward shock in the CSM, and hence, it can effectively mask the identity of the underlying SN ejecta spectrum (see, e.g., Smith et al. 2008a for more details).

Because of its relatively weak CSM interaction at early times, PTF11iqb affords an interesting opportunity to more clearly see the underlying SN II-P photosphere. The signature of a SN II-P is seen from the shoulder in the light curve, which can be explained as a composite of a normal plateau and CSM interaction, and the visible-wavelength spectrum toward the end of that plateau matches a SN II-L, when the

[8] We note one caveat, related to sensitivity or time resolution. An emission feature at ∼7100 Å identified by Gal-Yam et al. (2014) as N IV was strong in the spectrum of SN 2013cu taken 15.5 hr after explosion, but the feature faded beyond detectability by day 3 (see Figure 11). This feature was also seen in SN 1998S, although Leonard et al. (2000) identified it as a C II blend. Unfortunately, our earliest spectrum of PTF11iqb is too noisy at these wavelengths to see if the feature is present at the same level as in SN 1998S at a similar time.

[9] The estimate of $\sim$ 10 AU in the case of PTF11iqb comes from the required photospheric radius, given the observed luminosity and temperature we quote here. A radius of 10 AU is also consistent with the radius of the CDS on day 2 in our CSM interaction model. Gal-Yam et al. (2014) quote a similar approximate radius of 10^{14} cm.

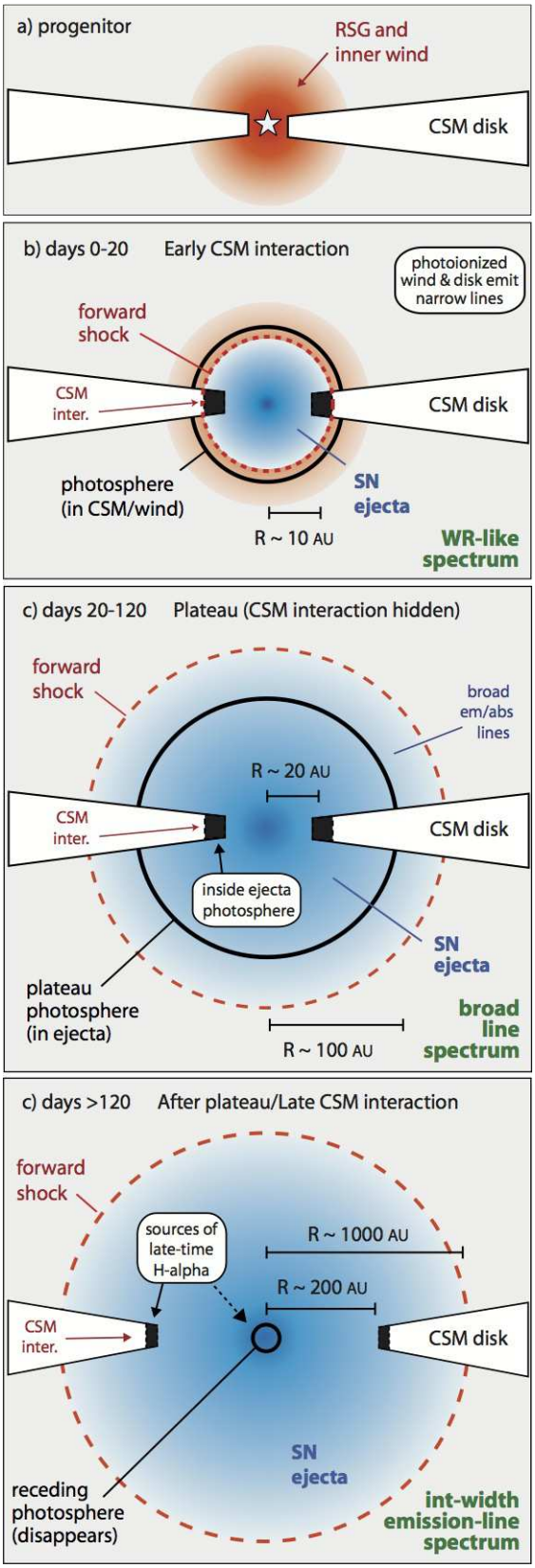

Figure 12. Illustration of a proposed sequence of events to account for PTF11iqb's evolution. The four panels (*a*–*d*) are discussed in the text, §8.

broad-lined SN ejecta dominate the observed light. Moreover, it seems clear from the composite SN II-P plus CSM interaction light-curve model that all one needs to do is "crank up" the CSM interaction by a factor of a few (in CSM density and luminosity) to make this object look like the more traditional SN IIn explosion SN 1998S.

When we first described the spectral evolution of PTF11iqb in §3.2, we highlighted three main phases:

(1) The early phase (days 0–20) dominated by a smooth blue continuum, narrow emission lines with broad Lorentzian wings, and the WR-like spectral features. During this time, the spectrum was that of an opaque wind ionised by either CSM interaction or a UV flash from shock breakout (or both).

(2) The plateau phase (days 20–120) when the spectrum resembled the broad-lined photospheric spectrum of a normal SN II-P or II-L, with broad emission and absorption profiles. In this phase, the emitted light is dominated by the fast SN ejecta, as in a normal SN.

(3) Late-time CSM interaction with strong asymmetric Hα, which can be subdivided into the early nebular phase (days 120–200) when Hα had a strong blueshifted peak and was probably powered largely by radioactive decay, and later times (after day 200) when Hα must have been powered by CSM interaction and had a stronger redshifted peak.

In Figure 12, we show a sketch that illustrates a proposed sequence of events to qualitatively explain this observed evolution of PTF11iqb. The four panels in this figure are described below.

Figure 12a: The progenitor is a RSG or yellow supergiant/hypergiant surrounded by a dense wind and an even denser disc-like distribution of CSM. The densest parts of the disc may reside at a radius of $\sim$ 10 AU. The disc is likely the remnant of some previous binary interaction events.

Figure 12b: For the first $\sim$ 20 days immediately after explosion, the SN ejecta crash into the inner dense wind of the progenitor at a radius of $\sim$ 10 AU. However, the wind is opaque once it is ionised, and a photoionised precursor (due to either CSM interaction X-rays that are reabsorbed, or to a UV flash from shock breakout) creates an electron-scattering photosphere outside the fast SN ejecta. Narrow lines are emitted by the preshock wind. The collision in the equator slows the expansion there, but the fast ejecta expand freely at other latitudes.

Figure 12c: At days 20–120, the radius of the SN ejecta photosphere has now grown to $\sim$ 100 AU at latitudes away from the equatorial plane, as in a normal SN II-P. Although the photosphere is constantly receding in mass coordinates through the expanding ejecta, it is larger than the radius where the most intense CSM interaction is occurring in the equator (10–20 AU). *Thus, the equatorial CSM interaction region is enveloped by and hidden inside the normal broad-lined SN photosphere as seen from most viewing angles.* This is the most likely explanation for the disappearing or weakening narrow lines in some SNe IIn. If CSM interaction still contributes to the total plateau luminosity, the photons must diffuse out through the fast ejecta.

Figure 12d: At late times after the plateau drop (days 100–120), the continuum photosphere recedes to smaller radii and once again exposes the CSM interaction occurring in the disc. As the photosphere recedes completely and the ejecta become optically thin, the emergent spectrum is

dominated by optically thin ejecta powered by radioactive decay plus CSM interaction in a disc or torus. The postshock speed of the swept-up CSM is a few 1000 km s^{-1}, indicated by the width of the multipeaked asymmetric Hα line.

This sequence of events gives a satisfactory explanation for the spectroscopic evolution seen in PTF11iqb. By changing the density and radial extent of the CSM disc (and perhaps also by changing the viewing angle of the observer) one can adapt this scenario to other SNe: with denser or more extended CSM, we get a SN IIn like SN 1998S, and with less dense or less extended CSM, we may get normal SNe II-L or II-P events. Thus, this scenario for PTF11iqb provides a direct bridge between SNe IIn and SNe II-P/L.

This, of course, does not mean that all SNe IIn are actually Type II-P explosions underneath their CSM interaction, but it does confirm that *some of them* are underlying SNe II-P that arise from RSGs or YSGs, although masked at some phases by CSM interaction. Most of the interest in SN IIn progenitors has thus far concentrated on LBVs, partly because in some cases the CSM mass is so high, and also because the very bright LBV-like progenitors may be easier to detect in pre-explosion data (Gal-Yam et al. 2007; Gal-Yam & Leonard 2009; Smith 2014; Smith et al. 2007, 2008a, 2010b, 2011c). Smith et al. (2009a) suggested that extreme RSGs like VY CMa have CSM environments that can produce lower-luminosity SNe IIn, and Mauerhan & Smith (2012) showed that the late-time CSM interaction in SN 1998S was consistent with such a wind operating for ~ 1000 yr before core collapse. More recently, Shivvers et al. (2014) have also found evidence for a RSG progenitor for SN 1998S based on very early high-resolution spectra, as noted above. There have been other suggestions of RSG progenitors of some lower-luminosity SNe IIn as well (Stritzinger et al. 2012; Smith et al. 2009b).

From the point of view of understanding the connection between SNe and their progenitors, an important question then arises: *For how long before explosion was PTF11iqb's progenitor a cool supergiant?* Extreme instabilities in the years leading up to core collapse are required to eject many $M_\odot$ in some cases that produce luminous SNe IIn, but there may also be less extreme instabilities that could drive a wind, cause violent pulsations, or simply inflate the star's envelope in the final years of a star's life (Smith & Arnett 2014; Quataert & Shiode 2012; Shiode & Quataert 2014; Ofek et al. 2014a). Yoon & Cantiello (2010) have also suggested that some luminous RSGs may experience an enhanced superwind phase for ~ 1000 yr before core collapse driven by pulsational instabilities. During most of its He-burning lifetime, the progenitor may therefore have looked quite different from how it looked in the decades or centuries immediately preceding explosion. Whatever the physical cause, it does seem clear that PTF11iqb resides between SN 1998S and normal SNe II-P in terms of its luminosity and CSM interaction intensity.

Thus, this type of pre-SN activity, instability, and variation in stellar structure may play an important role in understanding the connection between the most common core-collapse events (normal SNe II-P) and other objects like SNe II-L and SNe IIn that appear to have some overlap. It could be that SNe II-L and SNe IIn form a sequence of increasing progenitor mass and increased pre-SN instability (see, e.g., Yoon & Cantiello 2010), or perhaps it could be due to other factors, such as proximity of a companion star in binary systems that suffer these instabilities (Smith & Arnett 2014). Exploring the diversity in CSM density and geometry may be extremely important for sorting this out, since disc-like CSM around a RSG is unlikely without a companion star to supply angular momentum. As noted above, some objects classified as SNe II-L, including classic objects such as SN 1980K, SN 1979C, and others (see Fesen et al. 1999; Milisavljevic et al. 2012), do not have spectra obtained at very early times — perhaps they would have been classified as SNe IIn if they had been caught sufficiently early. Detecting additional cases like PTF11iqb and understanding how common they are may help flesh out the continuum of diversity in pre-SN mass loss. If there are additional weak SNe IIn that are not easily recognised because the SN IIn signatures are fleeting, it would imply that pre-SN instability is not limited to only 8–9% (Smith et al. 2011a) of core-collapse SNe that have been categorised as Type IIn.

ACKNOWLEDGEMENTS

We thank Iair Arcavi, Peter Blanchard, Yi Cao, Ori Fox, Paul Groot, Asaf Horesh, Michael Kandrashoff, Pat Kelly, Nick Konidaris, Rubina Kotak, David Levitan, Adam Miller, Yen-Chen Pan, Jarod Parrent, Paul Smith, and WeiKang Zheng for assistance with some of the observations and data reduction. We thank Eran Ofek for helpful discussions and assistance with the PTF photometric data. We thank the staffs at Lick, MMT, LBT, Keck, Palomar, and WHT for their assistance with the observations. Observations using Steward Observatory facilities were obtained as part of the observing program AZTEC: Arizona Transient Exploration and Characterization. Some observations reported here were obtained at the MMT Observatory, a joint facility of the University of Arizona and the Smithsonian Institution. This research was based in part on observations made with the LBT. The LBT is an international collaboration among institutions in the United States, Italy and Germany. The LBT Corporation partners are: the University of Arizona on behalf of the Arizona university system; the Istituto Nazionale di Astrofisica, Italy; the LBT Beteiligungsgesellschaft, Germany, representing the Max-Planck Society, the Astrophysical Institute Potsdam and Heidelberg University; the Ohio State University and the Research Corporation, on behalf of the University of Notre Dame, University of Minnesota and University of Virginia. The WHT is operated on the island of La Palma by the Isaac Newton Group in the Spanish Observatorio del Roque de los Muchachos of the Instituto de Astrofsica de Canarias. Some of the data presented herein were obtained at the W. M. Keck Observatory, which is operated as a scientific partnership among the California Institute of Technology, the University of California and NASA; the observatory was made possible by the generous financial support of the W.M. Keck Foundation. The authors wish to recognise and acknowledge the very significant cultural role and reverence that the summit of Mauna Kea has always had within the indigenous Hawaiian community. We are most fortunate to have the opportunity to conduct observations from this mountain.

N.S. received partial support from NSF grants AST-1210599 and AST-1312221. E.O.O. is incumbent of the Arye Dissentshik career development chair and is grateful to support by grants from the Willner Family Leadership Institute Ilan Gluzman (Secaucus NJ), Israeli Ministry of Science, Israel Science Foundation, Minerva and the I-CORE Program of the Planning and Budgeting Committee and The Israel Science Foundation. A.G.-Y. is supported by the EU/FP7 via ERC grant No. 307260, the Quantum Universe I-Core program by the Israeli Committee for planning and funding, and the ISF, Minerva and ISF grants, WIS-UK "making connections," and Kimmel and ARCHES awards. The supernova research of A.V.F.'s group at U.C. Berkeley is supported by Gary & Cynthia Bengier, the Richard & Rhoda Goldman Fund, the Christopher R. Redlich Fund, the TABASGO Foundation, and NSF grant AST-1211916. J.M.S. is supported by an NSF Astronomy and Astrophysics Postdoctoral Fellowship under award AST-1302771. K.M. is supported by a Marie Curie Intra-European Fellowship, within the 7th European Community Framework Programme (FP7). M.S. acknowledges support from the Royal Society. D.C.L. and J.C.H. are grateful for support from NSF grants AST-1009571 and AST-1210311, under which part of this research (photometry data collected at MLO) was carried out.

REFERENCES

Ahn C.P., Alexandroff R., Allende Prieto C., et al. 2014, ApJS, 211, 17
Arnett W.D., Meakin C. 2011, ApJ, 733, 78
Bloom J.S., et al. 2011, arXiv:1106.5491
Bramich D.M. 2008, MNRAS, 386, L77
Brown P.J., et al. 2009, AJ, 137, 4517
Byard P.L., OBrien T.P. 2000, Proc. SPIE, 4008, 934
Cenko S.B., et al. 2006, PASP, 118, 1396
Chandra P., et al. 2009, ApJ, 690, 1839
Chevalier R.A., Fransson, C. 1994, ApJ, 420, 268
Chevalier R.A., Irwin C.M. 2012, ApJ, 747, L17
Chugai N.N. 2001, MNRAS, 326, 1448
Cousins A.W.J. 1981, South African Astron. Obs. Circ., 6, 4
Crowther P.A. 2007, ARA&A, 45, 177
Corsi, A., et al. 2014, ApJ, 782, 42
Da Costa G.S. 1992, in Astronomical CCD Observing and Reduction Techniques, ed. S. B. Howell (San Francisco: ASP), 90
Dessart L., Hillier D.J., Waldman R., Livne E. 2013, MNRAS, 433, 1745
Elmhamdi A., et al. 2003, MNRAS, 338, 939
Faber S.M., et al. 2003, in Iye M., Moorwood A.F.M., ed., Proc. SPIE Vol. 4841, Instrument Design and Performance for Optical/Infrared Groundbased Telescopes. SPIE, Bellingham, p. 1657
Faran T., et al. 2014, MNRAS, 445, 554
Fassia A., et al. 2000, MNRAS, 318, 1093
Fassia A., et al. 2001, MNRAS, 325, 907
Fesen R.A., et al. 1999, AJ, 117, 725
Filippenko A.V. 1982, PASP, 94, 715
Filippenko A.V. 1997, ARAA, 35, 309
Firth R., et al., 2015, MNRAS, 446, 3895
Foley R. J., Smith N., Ganeshalingam M., et al. 2007, ApJL, 657, L105
Fransson C., Lundqvist P., Chevalier R.A. 1996, ApJ,461, 993
Fraser, M., et al. 2013, ApJ, 779, L8
Gal-Yam A. 2012, Science, 337, 927
Gal-Yam A., Leonard D.C. 2009, Nature, 458, 865
Gal-Yam A., Leonard D.C., Fox D.B., et al. 2007, ApJ, 656, 372
Gal-Yam A., et al. 2014, Nature, 509, 471
Gerardy C.L., Fesen R.A., Höflich P., Wheeler J.C. 2000, AJ, 119, 2968
Groh J.H. 2014, preprint, arXiv:1408.5397
Grundstrom E., et al. 2007, ApJ, 667, 505
Gutiérrez C.P., et al. 2014, ApJ, 786, L15
Heger A., Fryer C.L., Woosley S.E., Langer N., Hartmann D. H. 2003, ApJ, 591, 288
Horesh A., et al. 2011, ATel, 3512, 1
Johnson H.L., Mitchell R.I., Iriarte B., Wisniewski W.Z. 1966, Commun. Lunar Plate. Lab., 4, 99
Kiewe M., et al. 2012, ApJ, 744, 10
Laher, R.R., et al. 2014, PASP, 126, 941
Landolt A.U. 1992, AJ, 104, 340
Law N.M., et al. 2009, PASP. 121, 1395
Leonard D.C., Filippenko A.V., Barth A.J., Matheson T. 2000, ApJ, 536, 239
Leonard D.C., Filippenko A.V., Chornock R., Foley R.J. 2002, PASP, 114, 35
Levesque E., et al. 2014, AJ, 147, 23
Matheson T., et al. 2000a, AJ, 120, 1487
Matheson T., et al. 2000b, AJ, 120, 1499
Mauerhan J.C., Smith N. 2012, MNRAS, 424, 2659
Mauerhan J.C., Smith N., Filippenko, A.V., et al. 2013a, MNRAS, 430, 1801
Mauerhan J.C., Smith N., Silverman J.M., et al. 2013b, MNRAS, 431, 2599
Mauerhan J.C., Williams G.G., Smith N., et al. 2014, MNRAS, 442, 1166
Maund J.R., Smartt S.J. 2009, Sci, 324, 486
Milisavljevic D., et al. 2012, ApJ, 751, 25
Miller J.S., Stone R.P.S. 1993, Lick Obs. Tech. Rep. 66 (Santa Cruz: Lick Obs.)
Monet D.G., et al. 2003, AJ, 125, 984
Murase K., Thompson T.A., Ofek E.O. 2014, MNRAS, 440, 2528
Ofek E.O., et al. 2010, ApJ, 724, 1396
Ofek E.O., et al. 2012, PASP, 124, 62
Ofek E.O., et al. 2013a, Nature, 494, 65
Ofek E.O., et al. 2013b, ApJ, 763, 42
Ofek E.O., et al. 2013c, ApJ, 768, 47
Ofek E.O., et al. 2014a, ApJ, 789, 104
Ofek E.O., et al. 2014b, ApJ, 781, 42
Oke J.B., Gunn J.E. 1982, PASP, 94, 586
Oke J.B., Gunn J.E. 1983, ApJ, 266, 713
Oke J.B., Cohen J.G., Carr M., et al. 1995, PASP, 107, 375
Pan Y.-C., et al., 2014, MNRAS, 438, 1391
Parrent J., et al. 2011, ATel, 3510, 1
Pastorello A., Della Valle M., Smartt S. J., et al. 2007, Nature, 449,
Poole T.S., et al. 2008, MNRAS, 383, 627
Pozzo M., et al. 2004, MNRAS, 352, 457
Quataert E., Shiode J. 2012, MNRAS, 423, L92
Quimby R.M., et al. 2011, ATel, 3511, 1
Rahmer G., Smith R., Velur V., Hale D., Law N., Bui K., Petrie H., Dekany R. 2008, in Society of Photo-Optical Instrumentation Engineers (SPIE) Conference Series Vol. 7014
Rakavy G., Shaviv G. 1967, ApJ, 148, 803
Rau A., et al. 2009, PASP, 121, 1334
Roming P.W.A., Kennedy T.E., Mason K.O., et al. 2005, Space Science Reviews, 120, 95
Schlegel E.M. 1990, MNRAS, 244, 269
Schlegel D.J., Finkbeiner D.P., Davis M. 1998, ApJ, 500, 525
Schmidt B.P., et al. 1993, AJ, 105, 2236
Shiode J., Quataert E. 2014, ApJ, 780, 96
Shivvers I., et al. 2014, preprint, arXiv:1408.1404
Silverman J.M., Foley R.J., Filippenko A.V., et al. 2012, MNRAS, 425, 1789
Smith C.E., Nelson B. 1969, PASP, 81, 74
Smith N. 2013a, MNRAS, 429, 2366
Smith N. 2013b, MNRAS, 434, 102
Smith N. 2014, ARA&A, 52, 487
Smith N., Conti P.S. 2008, ApJ, 679, 1467
Smith N., Arnett W.D. 2014, ApJ, 785, 82
Smith N., et al. 2002, ApJ, 578, 464
Smith N., Li W., Foley R.J., et al. 2007, ApJ, 666, 1116
Smith N., Chornock R., Li W., et al. 2008a, ApJ, 686, 467
Smith N., Foley R.J., Filippenko A.V. 2008b, ApJ, 680, 568
Smith N., Hinkle K.H., Ryde N. 2009a, AJ, 137, 3558
Smith N., et al. 2009b, ApJ, 695, 1334
Smith N., Miller A., Li W., et al. 2010a, AJ, 139, 1451
Smith N., Chornock R., Silverman J.M., Filippenko A.V., Foley R.J. 2010b, ApJ, 709, 856
Smith N., et al. 2011a, MNRAS, 412, 1522
Smith N., et al. 2011b, MNRAS, 418, 1959
Smith N., et al. 2011c, ApJ, 732, 63
Smith N., et al. 2012, MNRAS, 420, 1135
Smith N., Mauerhan J.C., Prieto J.L. 2014, MNRAS, 438, 1191
Stetson P.B. 1987, PASP, 99, 191
Stetson P.B. 1991, in 3rd ESO/ST-ECF Data Analysis Workshop, ed. P.J. Grosbol & R.H. Warmels, ESO Conf. and Workshop Proc. No. 38 (ESO: Garching bei Múnchen), 187
Stritzinger M. et al. 2012, ApJ, 756, 173
Svirski G., Nakar E., Sari R. 2012, ApJ, 759, 108
Taddia F., et al. 2013, A&A, 38, 113
Utrobin V.P. 2007, A&A, 461, 233
van Dokkum P.G. 2001, PASP, 113, 1420
Van Dyk S.D., et al. 2013, ApJ, 772, L32
Van Dyk S.D., et al. 2014, AJ, 147, 37
Woosley S.E., Blinnikov S., Heger A. 2007, Nature, 450, 390
Yaron O., Gal-Yam A. 2012, PASP, 124, 668
Yoon S.C., Cantiello M. 2010, ApJ, 717, L62
York D.G., et al., 2000, AJ, 120, 1579
Zhang, T., et al. 2012, AJ, 144, 131